Ana Filipa Mendes Cristóvão

Licenciatura em Ciências de Engenharia Biomédica

3D Printing of Biocompatible Materials for Biomedical Applications

Dissertação para obtenção do Grau de Mestre em
Engenharia Biomédica

Orientador: Isabel Ferreira, Professora Associada, DCM-FCT/UNL

Coorientador: Ana Baptista, Investigadora Pós-Doutoramento, DCM-FCT/UNL

Júri:

Presidente: Prof. Doutora Carla Maria Quintão Pereira, Professora Auxiliar, FCT/UNL

Arguentes: Prof. Doutor Carlos Baleizão, Professor Auxiliar, DEQ – IST/UL

Vogais: Prof. Doutora Isabel Maria das Mercês Ferreira, Professora Associada, DCM - FCT/UNL

FACULDADE DE CIÊNCIAS E TECNOLOGIA
UNIVERSIDADE NOVA DE LISBOA

Junho, 2018

3D Printing of Biocompatible Materials for Biomedical Applications

À minha mãe, pelo apoio constante.

Acknowledgements

Gostaria, em primeiro lugar, de agradecer profundamente à minha orientadora, Professora Doutora Isabel Ferreira pela disponibilidade e incentivo durante todo o período da dissertação.

Agradeço também à minha coorientadora, Doutora Ana Baptista, pela disponibilidade, carinho e apoio disponibilizado a todo o momento.

À Professora Célia Henriques e ao Professor Alexandre Velhinho, por terem ajudado a valorizar este trabalho. O vosso contributo e conhecimento foi essencial.

Aos colegas de laboratório, sem os quais teria sido impossível desenvolver este trabalho. Pelo conhecimento partilhado, a entreajuda, as ideias brilhantes e a capacidade de resolver todo e qualquer problema.

Aos meus pais, pela motivação e por todas as oportunidades que me deram ao longo da vida. Pelo apoio incondicional e a confiança nas minhas capacidades.

Ao Rômulo, pelo amor incondicional, por me ajudar a ver a luz ao fundo do túnel e por toda a felicidade que me trouxe. Obrigada por teres dado o primeiro passo.

À minha Avó que, apesar de já não estar entre nós, continua no meu coração. Penso sempre no quanto gostava que pudesses ver o quanto cresci. Espero que estejas orgulhosa.

Aos amigos da faculdade, à Tabby por me ter trazido a melhor pessoa da minha vida, sem ti seria uma criança infeliz; às miguitas de sempre e para sempre: Anayza; Joana; Dalila; Daniela e Jéssica. Todo o vosso apoio e encorajamento é precioso.

Muito Obrigada!

Abstract

In this work, we develop and test materials to be used in a 3D printed prosthesis, made according to each patients' anatomy. These must be biocompatible, flexible and maintain airway permeability. Different polymeric materials based on PEGDA (polymer) and B2VT (photoinitiator) were studied, each with either PVA or SA and $CaSO_4$. These hydrogels were crosslinked with UV light, one while printing by extrusion and the other after being deposited in casts.

A systematic study was performed on the influence of laser power in in-situ reticulation and 3D printing of an SA and PEGDA/B2VT mixture, by testing their compression mechanical properties. This study was compared to samples with PVA, reticulated with UV light after 3D printing and the difference in terms of mechanical properties is enormous. First shows Young's Modulus in the range of 4-6 MPa and the second in the range of 0.8-1 MPa.

The results lead to the conclusion that higher percentages of PVA and B2VT increase the value of *E* and that the use of Alginate creates a material with a compression curve typical of foams.

Keywords: biocompatibility; hydrogel; 3D printing; UV radiation; Poly (ethylene glycol) diacrylate

Resumo

Neste trabalho desenvolvemos e testámos materiais a ser usados numa prótese tridimensional, impressa de acordo com a anatomia de cada paciente. Estes devem ser biocompatíveis, flexíveis e manter a permeabilidade das vias aéreas. Foram estudados dois tipos materiais poliméricos diferentes com base no polímero PEGDA e no fotoiniciador B2VT, utilizando PVA ou SA com $CaSO_4$. Estes hidrogéis foram reticulados com luz UV, um aquando da impressão tridimensional por extrusão e o outro depois de depositado em moldes.

Foi realizado um estudo sistemático sobre a influência da potência do laser aquando da impressão 3D e reticulação *in-situ* de uma mistura com SA e PEGDA/B2VT, recorrendo a testes de compressão para obter as propriedades mecânicas do material. Este estudo foi comparado com amostras com PVA, reticuladas com luz UV após impressão 3D. A diferença em termos de propriedades mecânicas é significativa, tendo o primeiro material um Módulo de Young num intervalo de 4 a 6 MPa e o segundo entre 0,8 e 1 MPa.

Os resultados obtidos mostram que maiores percentagens de PVA e B2VT aumentam o valor de *E* e que o uso de Alginato cria um material com uma curva de compressão típica de espumas.

Palavras-chave: biocompatibilidade; hidrogel; impressão 3D; radiação UV; polietilenoglicol diacrilato

CONTENTS

List of Figures

List of Tables

List of Abbreviations, Acronyms and Symbols

%	Percentage
3D	Three-dimensional
A	Samples Cross-Section
B2VT	RF with TEOHA solution
BAPO	Phenylbis (2.4.6-trimethylbenzoyl) phosphine oxide
$CaSO_4$	Calcium Sulphate
CMC	Cell-Mediated Control
CT	Computed Tomography
DLLA	D. L-Lactide
DMEM	Dulbecco's Modified Eagle's Medium
DMSO	Dimethyl Sulfoxide
DSC	Differential Scanning Calorimeter
E	Young's Modulus
F	Force
FTIR	Fourier-Transform Infrared Spectroscopy
g	Grams
l_0	Initial length
M	Molar Concentration
mL	Millilitre
mm	Millimetre
Mn	Molar Number
MPa	Mega Pascal

mW	Milliwatt
Mw	Molar Weight
N	Newton
NegC	Negative Control
nm	Nanometre
PBS	Phosphate Buffered Saline
PCL	Polycaprolactone
PEGDA	Poly (ethylene glycol) Diacrylate
PLMC	Poly (D. L-lactide-co-trimethylene carbonate)
PosC	Positive Control
PS	Polystyrene
PVA	Polyvinyl Alcohol
PVP	Polyvinylpyrrolidone
RCV	Relative Cell Viability
RF	Riboflavin
rpm	Rotations per minute
Rz	Resazurin
SA	Sodium Alginate
SBF	Simulated Body Fluid
SLA	Stereolithography
SMA	Shape Memory Alloys
SMP	Shape Memory Polymers
STD	Standard Deviation
TEOHA	Triethanolamine
Tg	Glass Transition Temperature
TMC	Trimethylene Carbonate
UV	Ultraviolet
UV-Vis	Ultraviolet-Visible Spectrophotometry
v/v	Volume/Volume
w/v	Weight/Volume

Δl	Samples Elongation
ε	Strain
λabs	Absorption Wavelength
λem	Emission Wavelength
μL	Microliter
σ	Stress

1

1 Introduction

1.1 Motivation

This work aims to develop polymeric materials that can be flexible but transform into rigid structures when at body temperature or in the presence of body fluids. To be used in biomedical applications, these materials need to be biocompatible, resistant and durable.

The approach followed here consists in trying to achieve a shape memory polymer with a transition temperature in the body temperature range and in creating a polymeric blend that can be printed in an extrusion 3D (three-dimensional) printer.

The 3D printing process involves the creation of a three-dimensional computational model formed by 2D layers, the extrusion (printing) of the layers through a computerized process and any post-processing techniques needed [1]. Using only lines and points, this process allows for the creation of a complex internal structure, building it up layer by layer. After each layer is completed, an ultraviolet light cures the already printed layers, allowing the object to become a cohesive structure. This process will allow the reproduction of custom prosthesis which is a great advantage compared to the existing prosthesis.

To counter the lack of materials that can be used in these prostheses, the scientific community is exploring new and biocompatible materials for bone, cartilage, arteries, pulmonary pathways, tendons, etc. The main motivation of the work was then to contribute to the development of new materials that can be printed and possibly implanted. This offered many challenges since literature is scarce in both the approaches considered; SMP (Shape Memory Polymers) or laser UV (Ultraviolet) curing combined with 3D printing pastes.

1.2 Objectives

This study sought to develop a polymeric material that enabled the creation of a three-dimensional prosthesis, exactly like the original anatomical structure. The material must necessarily be biocompatible, and flexible or rigid according to the medium. This was tried in two different approaches: one the development of a shape memory polymer with temperature transition in the range of 37 – 40 ºC and the second the development of materials that are flexible when printed but become rigid when in contact with an aqueous medium, while keeping their structural integrity. This was an exploratory study since literature is scarce when addressing these specific issues.

2

2 State of the Art

2.1 Implants and Prosthetic Devices

Tracheal stenosis is defined as an abnormal narrowing of the trachea, resulting in partial or total obstruction of the airways [2]. It occurs mainly due to complications caused by intubation or tracheostomy, although it may also be due to a congenital problem or caused by tumours. It can occur in multiple locations at once, although it is more common in only one place.

Clinical tracheal repair began in the 19th century and a few tracheal resections were cited at the beginning of the 20th century. After confirming that tracheal resections couldn't be performed when the excision extended 2 cm, surgeons started investigating the possibility of a prosthetic replacement. In the 1960s, the experimental investigation concluded that approximately half of the adult trachea could be removed surgically and reanastomosis performed [3]. This limit varies according to age, local anatomy, pathology and prior treatment. When a safe removal and reconstruction was not possible, a solid prosthesis was used. These created complications such as strictures, granulation, chronic infection, and dislodgement, which remained a problem with the development of porous prosthesis. The porous structure was developed to allow the connective tissue to grow, incorporating the prosthesis into the tracheal site. The most promising stents were made of silicone, such as the Neville prosthesis [4], although suture line granulomas remained problematic and were treated endoscopically[4][5].

Silicone endoprostheses are available in various shapes, lengths, and diameters. Some examples are shown in figure 1.1. The silicone T-tube has advantages in that it preserves upper airway permeability while the lateral branch is closed, maintaining the translaryngeal airflow to provide humidification, filtration, and heating of the inspired air, as well as preserving the voice [6]. This tube does not cause injuries to the tracheal wall and can be maintained for several

years. Other types of silicone prostheses are Y-tubes, characterized by the removal of the external lateral branch, maintaining only the Y bifurcation. There is also the Dumon Prostheses which has external protrusions on its external surface at 90 º, to prevent displacement.

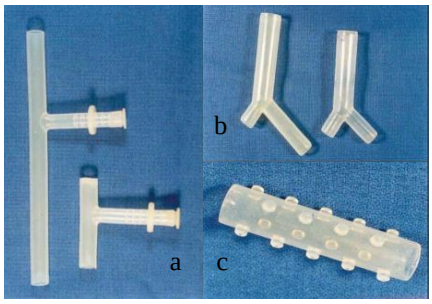

Figure 1. 1 – Silicone Airway Stents: (a) Montgomery's T-tube stent; (b) Y-tube stent; and (c) Dumon type stent [6]

Self-expanding metallic stents, as shown in figure 1.2, are more easily placed; however, their removal may result in serious complications. Usually, these prostheses are made of a nickel and titanium alloy (nitinol) and can be coated with a thin film of silicone. They are an evolution of regular silicone prostheses due to the lower radial force and accommodation to the irregular contours of the trachea. Unfortunately, these types of stents have frequent complications, including migration, particularly of silicone prostheses, or tissue growth between stent meshes. These can lead to blockage of the airway due to the accumulation of mucus and the consequent development of bacterial plaque. It is therefore obvious the need to create an innovative prosthesis that is adaptable to the needs of each patient, being able to solve the difficulties encountered.

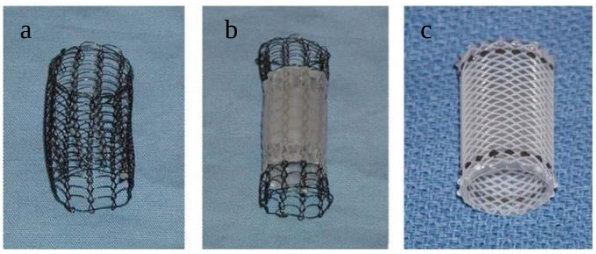

Figure 1. 2 – Self-expanding Stents: (a) Metallic uncoated stent (Ultraflex); (b) Metallic coated stent (Ultraflex); and (c) Reinforced Silicone stent (Polyflex) [7]

A recent study has piloted the use of a three-dimensionally printed artificial polycaprolactone tracheal graft coated with stem cells [8]. Studies using pericardium and aortic homografts have been shown to have good outcomes [9]. Another study demonstrated that silicone-stented aortic allografts have no cartilage regeneration [10], leading to proposals of a composite, fascial flap-wrapped allogeneic aortic graft with external cartilage ring support [11]. Homografts and allografts are both transplants of organs or tissues from one individual to

another of the same species, but the latter specifies that the individuals are of different genotypes. This approach could potentially be used to repair the trachea.

Today, the direct anastomosis is considered the best option [3][12], even though stenting and prosthetic reconstruction remain the primary methodology for larger defects. This direct approach uses the patient's own bronchial tissue while an ideal prosthesis made with a foreign material has not been developed. This ideal prosthesis is airtight, has the adequate consistency to prevent collapse, causes minimal to no inflammatory reaction, allows ingrowth of respiratory epithelium along the lumen and is impervious to fibroblastic and bacterial invasions of the lumen [13].

2.2 Memory Shape Materials

Memory shape can be defined as the property of a material that allows it to retain a temporarily altered shape until it is affected by a stimuli or trigger, which makes it return to its original shape. This stimuli or trigger can be temperature, moisture, magnetism, and ultrasound, depending on the sort of material used [14]. In a biomedical context, these materials can be divided between shape memory alloys (SMA) and shape memory polymers (SMP). SMA are out of context of this work so only SMP are described.

SMPs, are characterized by their glass transition temperature (*Tg*), demonstrate memory shaping properties through a mechanism inherent to their non-crystalline molecular structure, being characterized by a relatively low-temperature transition, within range of body and room temperatures, making them very suitable for biomedical applications [15]. However, to avoid inducing automatic shape change right after implantation, it is possible to use an SMP with transformation and transition temperatures slightly above body temperatures. This would create the possibility to regulate the shape change through a manual, on-demand thermal stimulus [14].

SMPs created through copolymerization of multiple monomers are also advantageous in the biomedical field due to their ability to target multiple complementary properties of interest [16], namely through control of the molar ratio between each monomer [15]

As an example of this, thermoreversible alginate hydrogels that under the effect of multiple simultaneous physical stimuli reverse to a gel form can be combined in order to target their specific mechanical and physical properties [16].

One characteristic of some SMPs is their relatively fast biodegradability, which actively contributes to their utility for biomedical applications and to the reduction of invasive surgeries due to the absence of the need to remove the implant [15]. SMPs can also be controlled through exposure to light or chemical reactions [15].

Even though SMPs are characterized by good short, medium and long-term biocompatibility, issues related to their chemical structure like their chemical stability or the additives used when mass producing each one of them still require further study and assessment before each can be selected for use in biomedical applications [15].

Another example of copolymerization would be the fabrication of scaffolds of biodegradable poly(D, L-lactide-co-trimethylene carbonate) (denoted as PDLLA-co-TMC, or PLMC) using electrospinning [14]. These scaffolds were expected to behave in a thermoresponsive and biomimetic manner, as this makes them advantageous in tuning the recovery temperature of the material to suit for shape memory applications in the human body. The degradation and mechanical properties of these scaffolds were found to be controllable through the variation of the molar ratio of DLLA (D. L-Lactide) and TMC (Trimethylene Carbonate) allowing them to vary between a glassy state to flexible and rubber-like elastomer [14].

In this balance between DLLA and TMC, the content of the latter in the PLMC had a large effect on the elasticity and resilience of the materials, with the higher TMC materials showing superior properties. The 56 and 70% TMC polymers showed constant tensile modulus and no plastic deformation after 10 000 continuous mechanical cycles, which is a considerable improvement over other similar materials [18].

Considering the properties of current biomimetic nanofibrous PLMC scaffolds associated with other desired functionalities such as biodegradability, bone forming ability, and shape memory effect in the desired *Tg*, the scaffolds may possess great potential for achieving very favourable outcomes in the course of scaffold-assisted bone repair and regeneration applications, [14] as it is demonstrated that a general approach to imparting both the shape memory and self-healing properties to chemically cross-linked hydrogels that otherwise do not have such functionalities [19].

The properties of the amorphous phase for the PLMC, namely the mobility of the former, are what determine the ability to deform the polymer's networks and to then fix the deformed networks.

The recovery of the macroscopic shape for the PLMC is described as a process where the chains of its networks change from an oriented network in their deformed state to their random coil conformations when they are reheated to a temperature above *Tg* [14].

SMPs can also be used in the development of biodegradable nanofibrous structures where they encompass both the biomimicking property of the nanofibers as well as the shape memory aspect of the SMPs, which gives them additional utility in the fields of tissue repair and regeneration [14].

2.2.1 Polymers

Hydrogels are cross-linked networks of hydrophilic polymers, usually with the capacity to absorb up to thousands of times their dry weight in water. Although their chemical stability is varied, hydrogels are usually biocompatible and can often be delivered into the body through minimally invasive methods [20]. They can be fabricated through several different methods, from radiating, freeze-thawing, chemical crosslinking or thermal annealing [21].

Although poly (vinyl alcohol) (PVA)'s stability as a gel is very thermally limited on its own, it has its mechanical properties enhanced when crosslinked with glutaraldehyde [15]. This process of ionic cross-linking is the frequently used method to obtain hydrogels from aqueous alginate solutions. It consists in combining ionic cross-linking agents like divalent cations with the alginate solutions [20].

The gel structure is created when, after the blocks of guluronate in the alginate chains are bound to the divalent cations, the former in one polymer chain form junctions with their equals in another polymer chain [20].

Although when it comes to ionic crosslinking alginate, one of the most used agents is calcium chloride ($CaCl_2$), it has the disadvantage of typically leading to gelation due to its high solubility in aqueous solutions.

Phosphate (e.g., sodium hexametaphosphate) is sometimes used to slow and control gelation, as phosphate groups in the buffer compete with carboxylate groups of alginate in the reaction with calcium ions, and slowing gelation.

Another approach includes using calcium sulphate ($CaSO_4$), which due to its lower solubility, can also slow the gelation rate and widen the working time for alginate gels.

When divalent cations are in use, the gel strength and uniformity become harder to control, making the gelation rate a critical factor in their regulation, as slower gelation produces more uniform structures and greater mechanical integrity.

The gelation rates, alongside the resultant mechanical properties of the gel, is affected by the gelation temperature. Crosslinking becomes slower, as the reactivity of the ionic crosslinkers is also reduced when temperatures are low.

Although there is a large variety in the mechanical properties of ionically cross-linked alginate, which varies according to its chemical structure, the resulting crosslinked network demonstrates greater order, leading to enhanced mechanical properties.

Alginates are usually stabilizing agents, as they help thicken and form a gel, effectively becoming very useful in drug administration, as the method of incorporation and the chemical structure of the drug may allow for multiple drugs to loaded into the alginate-based gel [20].

It is known that alginate is not degradable in the bodies of mammals, due to the lack of the necessary enzyme to cleave the polymer chains. However, using monovalent cations such as sodium ions that affect the cross-linking bonds existing in the gel, causing its dissolution [20].

When alginate is used for wound dressing, it maintains a physiologically moist micro-environment, minimizing bacterial infections at the wound site, consequently facilitating wound healing [20].

Alginate-based gels also show promising results for cell transplantation in tissue engineering, as the latter aims to provide man-made tissue and organ replacements to patients who suffer the loss or failure of an organ or tissue [20].

When precipitating alginate, either sodium or calcium chloride is added to the filtrate, resulting in alginic acid by treatment with diluted hydrochloridric acid. After further purification and conversion, water-soluble sodium alginate power is produced [20].

The physical properties of gels resultant from alginate are known to improve with the increase of the latter's molecular weight. This improvement only happens to an extent, as alginate solutions with too high molecular weights become undesirable for production due to their high viscosity [20], and consequent risk to damage the proteins and cells mixed in the solution [1]. However, this issue can be mitigated through the combined use of high and low molecular weight alginate polymers [20].

It is well known that not only could cross-linked polymers keep their original dimensions for a longer time during degradation, but that they are normally stable because the networks are invulnerable to the breakage of a single bond [22]. Considering this, a double-network polymer hydrogel composed of chemically cross-linked poly (ethylene glycol) (PEG) and physically cross-linked poly (vinyl alcohol) (PVA) has been used [19].

Compared to pure PVA hydrogel, with a tensile strength of only 0.17 Mpa at the ultimate elongation of 312%, the incorporation of chemically cross-linked PEG improves tensile strength by a large margin, in a gradually more prominent manner with the increasing PEG content [19].

Due to the almost constant elongation observed at the break, it is deduced that in the double-network hydrogel the physical network of PVA determines the limit of extension while the chemical network of PEG influences mostly the mechanical strength [19].

Polyethylene (glycol) Diacrylate (PEGDA) is a blank slate hydrogel that gels rapidly at room temperature in the presence of a photo-initiator and UV light. They are hydrophilic, elastic and can be customized to include a variety of biological molecules and are powerful tools for uncovering basic cellular biology because they are considered biologically inert and their mechanical properties can be varied over a large range of moduli.

2.2.2 UV Reticulation

Photoinitiated polymerizations have several advantages for polymer formation when compared to thermal or redox initiation mechanisms. The primary advantage is the control afforded over the temporal and spatial gelation process. Although simple in form, the polymerization behavior is complex because the propagation and termination rates are highly dependent on the conversion and evolving network structure [23]. Having conversion rates of approximately 100% is very important as low conversions may decrease the mechanical properties of the biomaterial. Not only that, but the non-reactive monomer may have damaging effects on the surrounding tissue.

Hydrogels created from photocrosslinking of hydrophilic PEGDA macromers are characterized by their ability to retain a large amount of water without dissolution and better biocompatibility. However, the use of UV radiation to prepare PEGDA hydrogels causes them to have poor mechanical strength [21].

A possible method to mitigate this weakness is to not only irradiate the components with UV radiation but to also subject them to a high energy electron beam followed by freeze-thawing [21].

PEGDA-based hydrogels prepared in the presence of polyvinyl alcohol (PVA) as a second component to enhance the mechanical properties of hydrogels, is desirable due to their biocompatibility and UV curability [21].

Due to the hydrophilic nature of PEGDA's macromers, possessing —C=C— bonds exist at their chain ends, these are easily used for photo-crosslinking among themselves, as the occurring radical polymerization leads to the formation of a solid network. Covalent bonds can be observed, due to the existence of chemical crosslinking's between themselves, while the connection between PVA and PEGDA is of physical crosslinks via hydrogen bonding [21].

An improvement upon the tensile properties of PEGDA-based hydrogels can be seen when PVA is added alongside irradiation by UV radiation, plus a high energy electron beam followed by freeze-thawing. This process can increase the hydrogel's crosslinking density and tensile strength when compared to other hydrogels prepared through similar methods [21].

Among the many methods PEGDA can be crosslinked, photopolymerization demonstrates varied applications in tissue-engineering applications. Photopolymerization presents the possibility to control the spatiotemporal parameters of polymerization, allowing the formation of rather complex shapes [24].

It is possible to produce substrates having mechanical properties with highly tuneable spatial parameters by using photolithographic patterning techniques and mixing under controlled conditions on PEGDA hydrogel polymers of different chain lengths

These substrates, characterized by their excellent biocompatibility, are favourable for the study of the interactions between cells and these substrates under varied conditions, presenting an improvement over the substrates patterned to date through mechanical methods [24].

The PEG molecule, known for being neutral [24], is considered to be inherently resistant to protein adsorption when crosslinked. Its characteristic mobility and high levels of hydration when in aqueous solutions are also considered to aid in this aspect, allowing PEG-based hydrogels to act as biologically inert materials [25]. One of these hydrogels, PEGDA may be useful as a model material for areas such as tissue restoration, wound dressings and vascular graft coatings [25].

Regarding the use of photopolymerization in biomedical applications, photoinitiators also require biocompatibility in order to be used, leading to the use of some molecules already found in biological systems which freely generate radicals.

One approach includes using Phenylbis (2.4.6-trimethyl benzoyl) phosphine oxide (BAPO) as it is a very potent photoinitiator. However, its use is severely limited due to its poor solubility in a variety of monomers and oligomers, as well as the added cytotoxicity associated with its combination with ethanol and acetone where it is soluble. These limitations make BAPO a questionable choice for use in biomedical applications [26].

Riboflavin or vitamin B2 is one of these biological photoinitiators, as flavins are known to be able to undergo reduction-oxidation reactions with rather ease. Riboflavin, excitable by photon absorption, can create either a triplet or a singlet-excited state. Due to riboflavin's incapacity to result in polymerization when alone in its triplet state, triethanolamine (TEOHA) was added to it as a co-initiator in order to mitigate this gap. This solution is viable due to what is believed to be the oxidization of the triplet state riboflavin by the TEOHA, which becomes semi-reduced while forming a semi-oxidized radical of riboflavin. The polymerization is caused by the existence of a neutral amine radical, created by the donation of a proton from the amine to the riboflavin radical [25].

Medical uses of riboflavin include the inactivation of pathogens in platelet concentrates when combined with UV light treatment and a contribution to the treatment of keratoconus through the induction of crosslinking of collagen within the cornea [25]. Its biocompatibility when in high doses or under UV exposure has already been shown, validating riboflavin as a biocompatible photoinitiator.

2.3 3D Printing in Biomedical Engineering

3D printing presents several health-related applications, namely in the fields of medicine and biology where its by-products are already in use in neurosurgery, orthopaedics, spinal

surgery, maxillofacial surgery [27], tissue engineering [1], indirect fabrication of medical devices [1], cell seeding and culturing [1], cardiac surgery and cranial surgery – where it can be used to directly print the final implant, amongst various other disciplines.

There is also use for 3D-printed in the context of studying more complex, hard to visualize cases, as well as teaching students and patients, or even allowing health professionals to practice certain procedures. These opportunities and others for the use of 3D-printed objects arise from the existence of certain surgical procedures which are currently complex enough to require a certain amount of guidance [27], which can be complemented by the fabrication of anatomical models for pre-surgical planning [1]. This is a requirement to avoid causing damage to certain essential parts of the body, considering current guidance requires the use of ionizing radiation in considerable amounts, lengthening the total surgical time.

In order to repair physical damage caused by other sources, namely some anatomical defects, using highly-customized prosthetics, there is a need for 3D printed objects with highly accurate measurements and properties [27].

2.3.1 Extrusion Printing

Extrusion-based 3D printing is an additive manufacturing technique which can be used for processing of paste-like materials into specific, three-dimensional shapes [28]. Hydrogels are a particularly important material and are frequently processed by extrusion-based 3D printing [29][30]. When compared to conventional processing techniques like moulding, 3D printing is better able to create complex objects.

In this type of printing, the material is charged into a reservoir and then pushed continuously through a nozzle with the appropriate size. A continuous strand of material is deposited onto the printer's bed. The object is then formed by the predetermined movements of the nozzle, done in a layer-by-layer method. The material's rheological properties determine its ability to flow and maintain shape fidelity.

Some of the hydrogels previously identified as suitable for extrusion-based 3D printing are PEGDA and alginate. These materials and others have been used to create aortic valve scaffolds [30], anatomically shaped cartilage structures like ears [31] and artificial blood vessels [32].

Despite the progress made, one of the still existing difficulties when printing hydrogels lies in creating an object with a significant height. Usually, these objects are just a few centimetres high because the stress imposed on the object during printing is higher than its mechanical stability, resulting in soft viscoelastic materials that cannot support themselves during processing.

2.3.2 UV Laser

After printing, viscoelastic materials are often subjected to post-treatment such as UV curing. This process converts the material into an elastic hydrogel [33] and has been used to create detailed PEGDA based aortic valves. The depletion of the acrylate end groups during radical photo-polymerization has an unknown effect on the bonds between individual layers of the printed object and thus on the mechanical properties of the object [28] [32].

In this work we use an extrusion-based 3D printer with an attached UV laser similar to the one used by Hiller et al. [28], focussing on the intermediate curing of cross-linked systems after the completion of each individual layer. Their work concluded that intermediate curing times (the sample was irradiated directly from above after each layer printed) facilitates the creation of taller objects, overcoming the yield stress limitations for non-cured hydrogels caused by gravitational forces. This same principle was used to create more homogenous objects in this work.

3

3 Materials and Methods

This chapter describes the methods and materials required to prepare polymeric solutions, the techniques used for UV reticulation and 3D printing, as well as those used to characterize the materials. This characterization was mainly focused on mechanical tests and cytotoxicity assays to evaluate the biocompatibility of the materials developed.

3.1 Materials and Methods

Table 3.1 summarizes the reagents used in the polymer mixtures, the variable parameters for each mixture and the protocol followed.

Table 3. 1 - Reagents used in the Protocols Performed and respective Variations

Polymer mixture		
Mixture	Protocol	Variations
A: PEGDA, BAPO, SA, $CaSO_4$	10 μL and 20 μL were added at a time to a total volume of 2 mL (1 mL PEGDA at 28.57 % v/v and 1 mL SA at 5 % v/v)	2 % or 1.5 % BAPO in ethanol (300 - 750 μL); 0.07 M $CaSO_4$ (210 - 630 μL)
B: PEGDA, B2VT, SA, $CaSO_4$	2.5 mL PEGDA 34.78 % w/v	0.15 mL to 0.75 mL B2VT and ($CaSO_4$ + 0.75 mL) from 0.0036 to 0.0081 g
C: PEGDA, BAPO, PVA	PEGDA 28.57 % v/v and 1 mL PVA at 20 % v/v; $CaCl_2$ 150 μL at 0.07 M	With or without 150 μL BAPO 1.5 % or 0.01, 0.03 g BAPO dissolved in 2 mL PEGDA
D: PEGDA, B2VT, PVA	2 mL PVA 5 %, 15 % or 25%; 2 mL PEGDA 34.78 % w/v	0.3 - 0.5 mL B2VT

The mixtures tested are based on PEGDA, a biopolymer soluble in water, BAPO, a photo-sensible polymer which is used to reticulate PEGDA and confers insolubility to water and so, rigidity. To demonstrate that PEGDA can be reticulated, BAPO was first used despite not being biocompatible. It was then replaced by B2VT (B2 Vitamin) when Riboflavin and TEOHA were available in the laboratory. The B2VT is a solution comprised of 4.3 mM of RF (Riboflavin) and 4.2 M of TEOHA. This photoinitiator had already been used with PEGDA in previous studies [25].

Preparation of B2VT solution (10 mL solution): 0.0095 g of RF; 3.1290 g of Triethanolamine (TEOHA); 10 mL of ultrapure water. Carefully weigh the RF and TEOHA in separate containers; 5 mL of ultrapure water was added to each container; A magnetic stirrer was placed in each container and the solutions were kept at room temperature; After 30 minutes of stirring, the two solutions were mixed and stirred for another 30 minutes.

Preparation of PVA solutions: in an Anton Paar Microwave Synthesis Reactor Monowave 400: the corresponding mass of PVA is placed in the reaction vessel (glass vial G30) along with a magnetic stirrer and 10 mL of purified water. This vessel is then placed inside the microwave where it is heated up to 180 ºC in 5 minutes (850 W, 1200 rpm – rotations per minute); it is maintained at that temperature for 10 minutes and then cooled down to 70 ºC (figure 3.1).

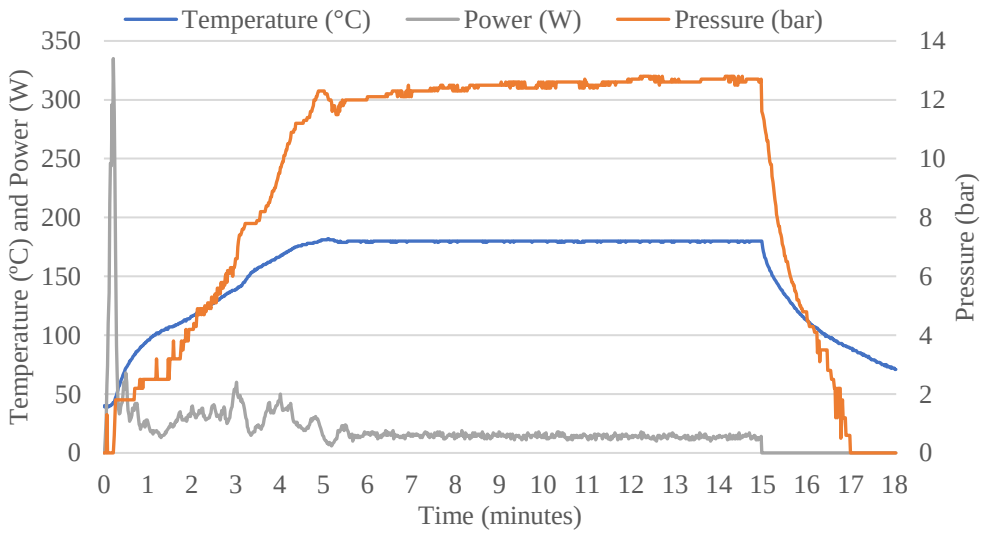

Figure 3. 1 – Example of a PVA reaction where the temperature, power, and pressure are shown during the reaction period

Preparation of Mixture B: 0.0108 g of $CaSO_4$; 1 mL of ultrapure water; 2.5 mL of 34.78 % w/v PEGDA solution in purified water; 2.5 mL of 5 % v/v Sodium Alginate (SA) solution in purified water; 1 mL of B2VT solution. Carefully weigh the $CaSO_4$, add 1 mL of ultrapure water, add 2.5 mL of the PEGDA solution while constantly stirring with a mixer, add 2.5 mL of the SA solution; keep stirring; finally, add the B2VT solution; the mixed liquid into a 20 cc syringe and

let it rest in an upright position for at least one hour and up to 12 hours. This allows the liquid to gelify slowly, becoming denser and acquiring the perfect density to extrude.

Reticulation of B Mixtures is done under UV laser (435- 455nm) at several different powers and between each printed layer in the extrusion 3D printer.

Preparation of Mixture C and D: To achieve a mixture that reticulates well under UV light, the ingredients (as determined in Table 3.1) must be mixed together at a temperature of approximately 80ºC and maintained at that temperature for the initial stages of reticulation to avoid deposition. Maintaining such temperature becomes more important as the desired thickness of the film increases.

Reticulation of A, C and D Mixtures is done under UV light with the aid of a UV nail lamp which emission spectra is represented in figure 3.2.

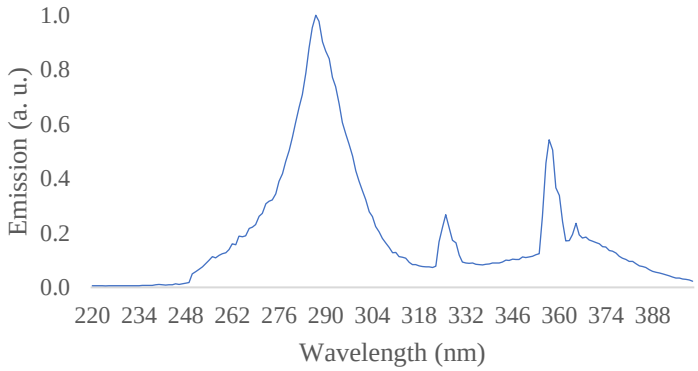

Figure 3. 2 - Emission spectra of UV lamp used to reticulate D type samples

According to previous studies, a mixture of PEGDA/B2VT has two UV-Vis (Ultraviolet-Visible Spectrophotometry) absorption peaks at approximately 350 nm and 450 nm [25] and saturates at wavelengths under 300 nm. This means that the UV lamp used is adequate for the photo reticulation of PEGDA/B2VT based materials.

3.2 3D printing

A 3D model was developed from the patient's Computed Tomography (CT) scan. The information retrieved from the scan is rebuilt through the files in DICOM® (Digital Imaging and Communications in Medicine) format and should be saved in .stl format, used for 3D printing, and then G-code, the language that contains all the instructions for the 3D printer.

The original files received included a model of the patient's upper body as shown in figure 3.3 (a). The file was modified in Blender, a software used for creating 3D models until only a

section of trachea was left (figure 3.3 (c)). This final file was then saved in a .gcode format using Cura 2.4.0.

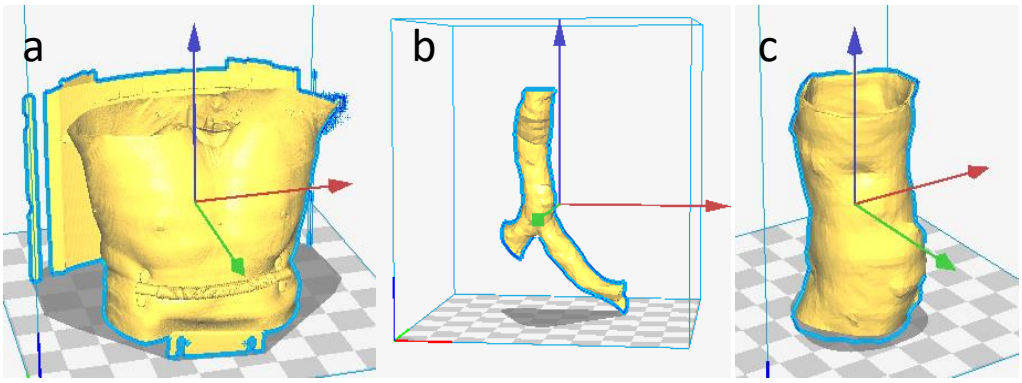

Figure 3. 3 - 3D models in .stl format based on the patient's CT scan: (a) initial model received; (b) model after some modifications; (c) model ready to print

The .gcode file was then altered using a software previously created by former FCT-UNL student Filipe Silvestre, that incorporated a UV laser layer between each printed layer. This results in each new layer being reticulated and vulcanized to the layer beneath it when printing. Two objects are shown in each image in figure 3.4. This is because one corresponds to the printed object (right on image (a)) and the other corresponds to the laser reticulation layers (left on image (a)). The laser has a -70 mm offset on the y-axis due to the way the printers' head was built.

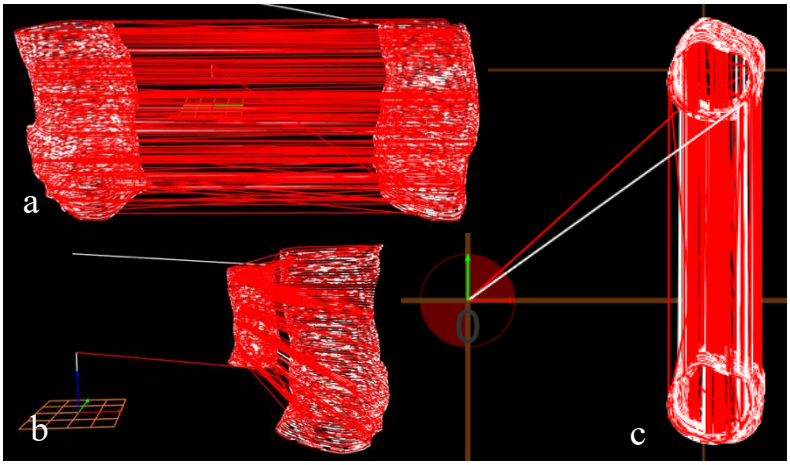

Figure 3. 4 - 3D models in .gcode format with intercalated laser layers: (a) view from the right; (b) front view; (c) top view

Other, more simple objects were created using the same methodology to test the materials' mechanical properties. These .gcode files were saved in a memory card that was placed in the printer's computer. The objects were printed by extrusion and left to dry until completely solid.

The extrusion printer had been previously custom made for the laboratory and can intercalate UV laser reticulation between each printed layer. Due to the use of this ability, the printer's original bed was replaced with a marble one.

Since the goal was to 3D print an object and since the mixture had to be reticulated with UV light, several laser powers were tested to find the most appropriate. Another important issue was deciding what bed to choose when printing, seeing as the laser could damage the original bed at a higher power. A base of marble was chosen as it does not burn, provides a stable and solid base for printing and absorbs any excess water caused by higher humidity in the room, providing better adhesion for the first printed layer.

The objects printed were designed with Blender and Cura 2.4.0, which creates a G-code file later read by the printer. In this file, the laser power is determined by a number between 0 and 255 which corresponds to 0 mW and 4000 mW, respectively. Table 3.2 shows this correspondence. Laser powers will be represented by the corresponding G-code values from here on out. This laser emits in a range between 435 and 455 nm, with a maximum power of 3.8 W, which means it includes one UV-Vis absorption peak of PEGDA/B2VT [25].

Table 3. 2 – G-Code values and corresponding laser power

G-Code	0	1	5	10	15	20	30	40	50	60	70	80	90	100	255
mW	0	16	78	157	235	314	471	627	784	941	1098	1255	1412	1569	4000

3.3 Tension and Compression Tests

Tension and compression tests were performed to understand how influential the different components are to the mechanical properties of the two materials, the impact of increasing PVA percentage in the PEGDA membranes, as well as how the laser power during reticulation affects those properties.

Several samples were subjected to tensile testing to determine an average Young's Modulus/ Modulus of Elasticity and maximum Elastic Deformation.

Tensile tests were performed on a Rheometric Scientific traction machine, Minimat Firmware 3.1, with a load cell of 20 N and speed of 2 mm / min. Compression tests were performed on this same traction machine and on a Shimadzu AG-50kNG mechanical testing machine at 0.5 mm / min.

Two types of compression tests were performed on printed samples. First, the force was applied perpendicularly to the printed layers; these tests were called Perpendicular. In a different set of samples, the force was applied parallel to the printed layers; these tests were called Parallel.

3.3.1 Stress-Strain Curves

A typical tensile curve is shown in figure 3.5, where two different zones are presented. The elastic zone is represented by a straight line while the plastic zone starts after the yield point and is represented by a curve. The Young's Modulus (E) corresponds to the tangential line of the points belonging to the elastic region and represents the strength of the material against elastic deformation (ε).

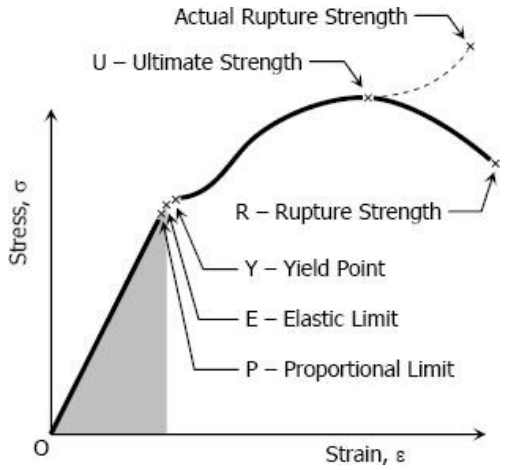

Figure 3. 5 – Stress-Strain Diagram [34] **Retrieved 2 April 2018**

The stress-strain curves resulting from the compression tests are similar to those shown in figure 3.6, in which three main zones are distinguished: elastic zone, collapse plateau, and densification zone. The elastic phase corresponds to the bending of the foam walls, followed by the collapse phase when the cell walls are damaged or fractured. Finally, the densification zone is characterized by increased tension and crushing of the cell walls.

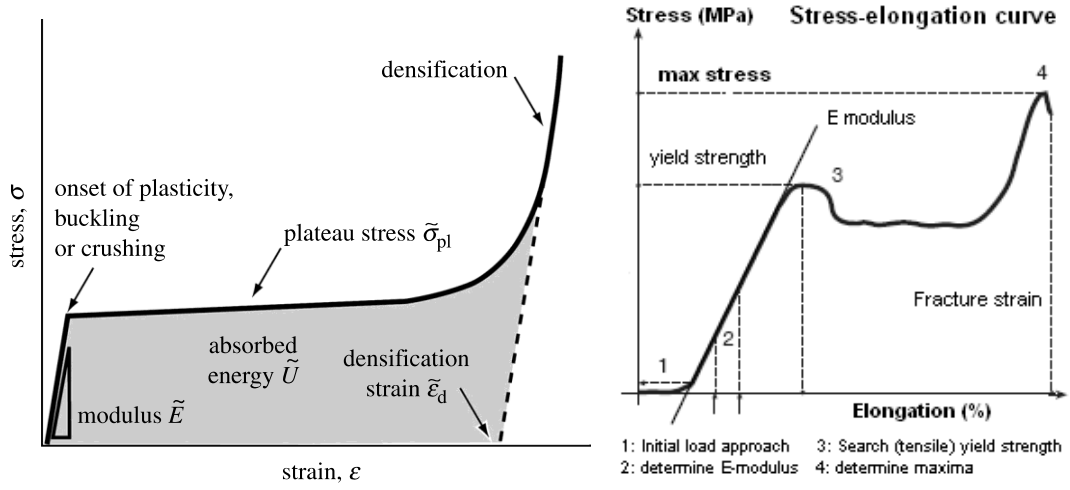

Figure 3. 6 - Typical Compression Curve for Foams [35] (left) and for polymers [36] (right) Retrieved 2 June 2018

Elasticity Modulus, also known as Young's Modulus is equal to the longitudinal stress divided by the strain. It measures the materials ability to withstand changes in length when under lengthwise tension or compression. Stress (σ) is calculated by dividing the applied force (F) by the samples cross-section (A) and Strain (ε) is calculated by dividing the samples elongation (Δl) by the samples initial length (l_0).

The strain was calculated considering the continuous changes in each samples length. First, the nominal extension (*ext*) at any given time was calculated by dividing the current length by the initial length. Then, ε was calculated by applying the natural logarithm to that extension plus one:

$$\ln(1 + ext)$$

The stress at any given time was given by:

$$\left(\frac{1000 \times F}{A}\right) \times (1 + ext)$$

where F is the applied force in kN and A is the area of the samples cross-section in mm^2. With these values, we could create a stress-strain curve and calculate the value of the first slope for each sample, therefore calculating E. The stress-strain curves presented for each sample are the ones given directly by the tests.

Young's Modulus (E); Maximum Stress; Maximum Strain; Maximum Force and Initial Distance between claws are presented for each Tensile test. In addition, the Average value and standard deviation (STD) for each type of sample are also presented, as is an Average* and respective STD* when outlier values were removed.

3.4 Fourier-Transform Infrared Spectroscopy – FTIR

The irradiation of a sample with infrared radiations within a specific range of wavelengths leads to an excitation of its molecular structures into a higher vibrational state. Each molecular structure possesses inherent wavelength values associated with this transition from an at-rest state to an excited vibrational state. It is possible to create a function that associates the energy difference in this transition with said inherent wavelength value. The absorption bands visible in these functions, with wavelength values characteristic to certain molecular components and structures, allow for their identification in the resulting function. To obtain an informative spectrum of intensity as a function of wavelength, a Fourier-Transform is performed over the interferogram created previously along the process of FTIR spectroscopy.

3.5 Ultraviolet-Visible Spectrophotometry – UV-Vis

UV-Vis is the application of spectroscopy, regarding either reflectance or absorbance, as is the case in this study, within the spectral region of the ultraviolet-visible. This spectroscopy is performed by irradiating the molecular structures within a specific wavelength range, where certain non-bonding electrons can be excited to higher molecular orbitals through absorption of energy. The resulting wavelength at which an electron is excited depends on how easily this orbital transition can be performed.

3.6 Cytotoxicity

Cytotoxicity was tested using *Vero* cells: African green monkey kidney epithelial cells. The cell culture was done in 96-well plates in culture medium DMEM (Dulbecco's Modified Eagle's Medium, Sigma-Aldrich D5030). Cultures were kept in the incubator (37ºC, 5% CO_2, SANYO CO_2 incubator, Model HCO-19AIC (UV)). A Trypan Blue solution (0.4%, Gibco®, Invitrogen™) was used to facilitate cell count. Resazurin (Alfa Aesar, USA) at 0.2 mg/mL in PBS (Phosphate Buffered Saline) was used for the colourimetric tests whose absorbances were measured in the microplate reader (Biotek ELX 800 UV). DMSO (Dimethyl Sulfoxide, M = 78.13 g mol^{-1}, MERCK-Schurardt) was added to the positive control wells.

In vitro cytotoxicity tests were performed using the extraction method. This consists of obtaining an extract of the sample by placing it in culture medium and then replacing the medium used to grow the cells with this conditioned medium.

The procedure followed in the cytotoxicity tests was as follows:

- In the first test, the samples were sterilized using ethanol. Both samples were submerged in approximately 2 mL of ethanol 70% (v/v) and left there for 48 hours. They were removed and left to air dry in a sterile environment for 24 hours and then irradiated with UV light for 30 minutes. In the second test, the samples were also sterilized using ethanol but were submerged for only 5 minutes and left to dry for 24 hours and then irradiated with UV light for 30 minutes.
- In the first test, the medium was added to each sterilized sample to have a 15% w/v ratio. This main solution was then diluted to create 10% and 5% w/v ratios. In the second test, the original solution had a 20% w/v ratio and was diluted to obtain 15%, 10%, and 5% w/v ratio solutions.
- Cells were trypsinized and suspended. Trypsin is an enzyme capable of cleaving the bonds between the amino acids of the intercellular proteins responsible for their adhesion to surfaces, leaving them in suspension.

- Cells were then seeded in a 96-well plate with adequate cell density and allowed to multiplicate for 24 hours in the incubator (37ºC, 5% CO_2, SANYO CO_2 incubator, Model HCO-19AIC (UV)).
- The culture medium of each well was replaced by the conditioned medium in each concentration to be tested. Five replicas were done per concentration of each sample as well as per control. Positive, Negative and Cell-Mediated Controls (CMC) were performed on each plate, serving as a reference to calculate viability. The cells were incubated under these conditions for 24 hours.
- The conditioned medium was removed and a Resazurin solution 10% (v/v) was added to the culture medium. To each well were added 120 µL of medium with Resazurin. The cells were incubated for 3 hours, after which the absorbance measurements were done to calculate viability.

The viability of the cells is measured using a colourimetric method based on the colour of the reagent Resazurin, which is blue (λabs = 604 nm) with no fluorescence and turns pink when reduced to Resorufin (λabs/ λem = 571/585 nm) by living cells. Fluorescence measurements allow us to quantify the number of living cells and know the samples toxicity.

Two extraction tests were done for each type of sample (Protocol B and Protocol D) to verify the accuracy of the obtained results since they were different from those expected. This is also why in the second test the samples were not submerged in ethanol. In the first test, CMC was not replicated due to lack of medium. In the first test, the positive control was done once at 10% DMSO while in the second test there were two positive controls, one at 10% DMSO and one at 20% DMSO. This was done to give us a better understanding of the toxicity of the material when compared to the positive control

The schemes of the plates used in the different tests are represented in tables 3.3 and 3.4.

Table 3. 3 - Plate preparation for the first cytotoxicity test

	1	2	3	4	5	6
A	Positive Control					CMC
B	Negative Control					
C	15%	Protocol B C5B				
D	10%					
E	5%					empty
F	15%	Protocol D D5A				
G	10%					
H	5%					

Table 3. 4 – Plate preparations for the second cytotoxicity test

	1	2	3	4	5	6	7	8	9	10	11	12
A	20%	15%	10%	5%	20%	15%	10%	5%	Negative Control	Positive Control: DMSO 10%	Positive Control: DMSO 20%	CMC
B	Protocol B C5A				Protocol D D5B							
C												
D												
E												

4

4 Result Analysis and Discussion

This chapter shows the main results and includes the discussion of tests related to the development of shape memory polymers, the polymer mixture for 3D printing and their mechanical and compositional analysis, including cytotoxicity assays.

4.1 Shape memory polymer

A first approach to develop a shape memory polymer was performed with a copolymer seeking the following characteristics: shape memory with glass transition temperature around 37ºC; biocompatibility; possible 3D print; high elasticity/flexibility; possible biodegradability, and anti-bacterial properties.

From the literature, we found a copolymer that could fit these features. PLMC was synthesized with the goal of attaining shape memory effects using DL-Lactide (DLLA) (99%, Alfa Aesar) and Trimethylene Carbonate (TMC) (99.5 %, Mw 102.09, Actu-All Chemicals) according to a report from literature [15]. PLMC is a biocompatible and biodegradable semi-crystalline polymer also known as Poly (D. L-Lactide-co-TMC). It was synthesized at an 8:2 DLLA: TMC ratio using Tin(II) 2-ethyl hexanoate (Stannous Octoate) (92.5 %, Mw 405.12, Sigma-Aldrich) as a catalyst, as suggested in previous studies [14]. Polystyrene (PS) (melt index 2.0 - 4.0 g/10 min, Sigma Aldrich) and Polycaprolactone (PCL) (Mn ~ 80,000, Sigma-Aldrich) were added to PLMC and tested for shape memory properties.

Thermal properties of PLMC have been shown to change according to their DLLA: TMC ratio with only one glass transition having been detected in their DSC (Differential Scanning Calorimeter) curves. It has been shown that for an 8:2 weight ratio, the glass transition temperature is 36.7 ºC [14]. The polymerization of PLMC (8:2) was done according to the protocol defined in previous studies [37]. It was performed in a 500 mL single-neck flask with constant use of a magnetic stirrer. Stannous Octoate (SnOct) 1.5 ‰ (g/g) was used as a catalyst for the reaction. After placing all elements in the flask, it was filled with nitrogen and degassed in vacuum three times, then sealed. The flask was then immersed in an oil bath at 100 ºC until the reactants melted. The oil bath was then increased to 130 ºC, always under magnetic stirring, and kept at that temperature for 12 hours. This time was determined by trial and error since the

original article indicated 5 hours while others indicated 48 hours. The polymer was then removed from the flask by dissolution in chloroform, purified by precipitation in methanol and then dried under vacuum.

Several tests were done where PLMC would be submerged in heated water and given a shape, then put in the freezer at approximately 0ºC and finally submerged again in water at the same initial temperature. The best results were obtained at 39.8 ºC when the sample exhibited shape memory properties. Varying the monomer ratio of DLLA: TMC it's possible to reach a glass transition temperature of 37 ºC. Unfortunately, due to the physical characteristics of the polymer, it could not be used in a 3D printer.

Polystyrene (PS) was added to PLMC and a film was produced which exhibited shape memory properties at 70.8 ºC in water (figure 4.1 (a)); when PCL was added, a film was produced with shape memory properties at 50 ºC.

To better test its shape memory properties, the samples were dissolved in DCM: DMF and alternately dried under vacuum and heated at 60 ºC.

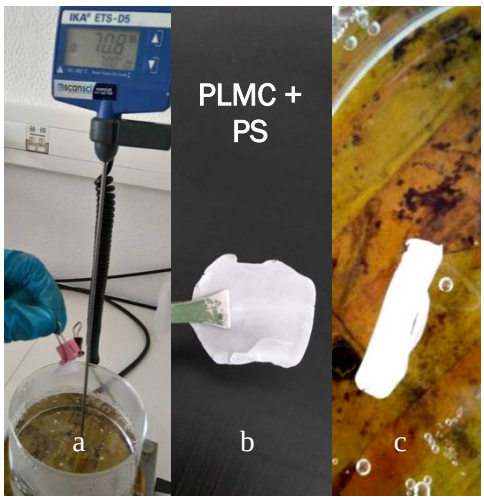

Figure 4. 1 – Testing PLMC/PS shape memory properties: (a) Initial Shape; (b) Deformed Shape; (c) Recovered Shape

As the results achieved did not present the envisioned phase transition at 37- 40 ºC and since the PLMC synthesis is very expensive, another approach was tested, focusing on the development of a polymer able to be printed in an extrusion 3D plotter.

4.2 Polymers mixtures and 3D printing tests

This section shows the results obtained with different mixtures of polymers with the objective of finding a mixture with good consistency to print, enabling the 3D printing of a complex piece.

4.2.1 Polymer mixture A

A mixture of **PEGDA**, as the base polymer, **SA**, as a thickener, **BAPO** and **$CaSO_4$** was tested to achieve a printable material that would reticulate under UV light – polymer mixture A.

In a first step, several concentrations of $CaSO_4$ were tested in a mixture with PEGDA (1 mL at 28.57% v/v) and SA (1 mL at 5% v/v), to achieve a printable paste. The best results were achieved with 120 µL of $CaSO_4$ solution at 0.06 M. The paste did not seem grainy and lines printed maintained shape and consistency. The use of 130 µL of a solution at 0.08 M also wielded good results while with 90 µL of a solution at 0.1 M the paste was too dense and grainy to print properly.

The hand printed structures were left overnight at approximately 10ºC for 12 hours, appeared to have shrunk slightly and had lost some water. Elasticity was maintained although they remained too fragile to handle. This was expected since no photoinitiator was added.

Small tubes were made in an extrusion-based 3D printer and left in the open for 24 h. The 0.06 M sample formed some air pockets in the syringe but the structure printed at 700 rpm maintained its shape, deforming only because of the printer bed instability. The 0.08 M sample was run at 500 rpm and did not seem homogenous. Sample 0.1 M was too dense to print and did not maintain an aggregated structure. In figure 4.2 we can see the results after 24 hours. Sample 0.06 M lost the most amount of water, while sample 0.1 M seemed to not have lost any water. Sample 0.08 M didn't lose too much water but had difficulties maintaining stability. Due to these results during and after printing, it was decided to test different concentrations of the photoinitiator with a solution of 0.07 M of $CaSO_4$.

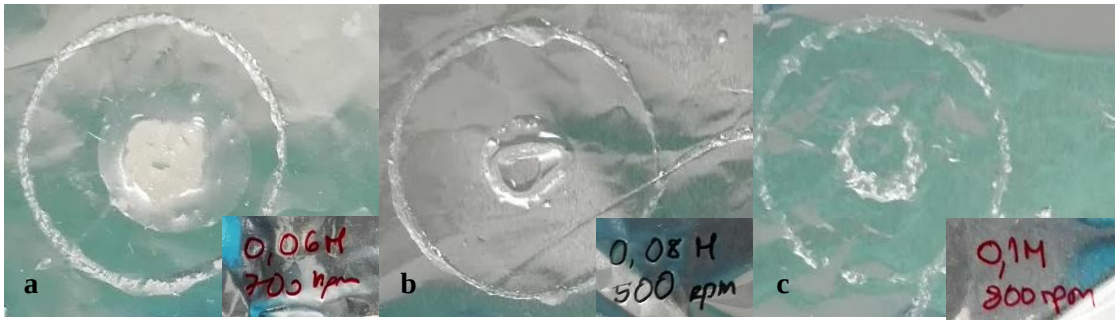

Figure 4.2 – Samples with different concentrations of $CaSO_4$, 24 hours after being 3D printed – top view: (a) 0.06 M, (b) 0.08 M and (c) 0.1 M

In the second step, the photoinitiator was added to the mixture and several concentrations of BAPO and $CaSO_4$ were tested as shown in table 4.1. Between 10 μL and 20 μL of BAPO and $CaSO_4$ were added at a time to a total volume of 2 mL (1 mL PEGDA at 28.57% v/v and 1 mL SA at 5% v/v), until the pre-determined volume was reached in each test sample. These samples were observed to determine the subsequent trials. These observations led to sample 14 being deemed good enough to start printing trials.

When PEGDA was tested with only BAPO (2 mL at 28.57% and 600 μL at 1.5%, respectively), the result was too liquid and it lacked elasticity.

Table 4.1 - Different concentrations of BAPO tested: 2mL PEGDA (28.57%) and 2mL SA (5%)

Sample	BAPO in Ethanol (μL)	$CaSO_4$ (0.07M) (μL)	BAPO/$CaSO_4$		Result
			BAPO 2%	BAPO 1.5%	
3	750	630	1.19		The paste was too dense to print.
4	690	570	1.21		Loses too much water when reticulating. Doesn't reticulate all the hydrogel.
12	750	600		1.25	Less elastic than sample 9.
13	690	540		1.28	More liquid than expected. Could not maintain printed shape.
2	600	450	1.33		Not fluid enough to print
9	600	450		1.33	Wasn't fluid enough to print may have had solid particles blocking the needle.
5	450	330	1.36		Printed at 1200 rpm. There were solid pieces already before printing.
7	450	330		1.36	Still losing too much water when reticulating.
8	540	390		1.38	Still losing too much water when reticulating.
1	300	210	1.43		Needs more $CaSO_4$.
6	300	210		1.43	Is too liquid before printing and so it loses too much water.
14	600	390		1.54	Reticulated after 2.5 hours under UV light; displays some elasticity; has kept the original shape and size. Prints well on paper after being centrifuged.
15	600	330		1.81	Too elastic. Doesn't attach itself correctly to the printing bed.

The different solutions presented in table 4.1 were tested in a first approximation by hand printing, they were then reticulated under UV light. The consistency of both the solutions and printed pieces was observed. The best solution from this set of trials was sample 14. In figure 4.3 we can observe some of the printed samples, comparing the pictures with the results stated in table 4.1.

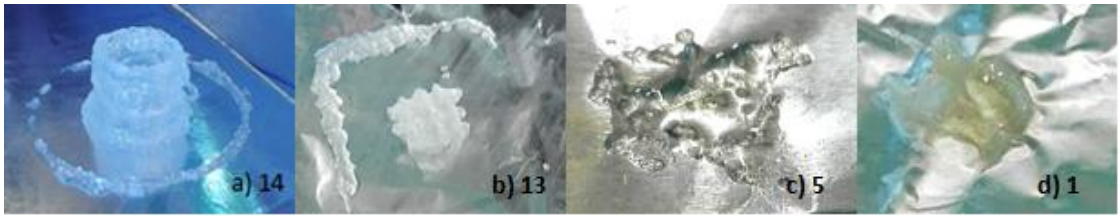

Figure 4. 3 - Examples of some of the samples printed including (a) sample 14, (b) sample 13, (c) sample 5 and (d) sample 1

A solution with the same composition of sample 14 was used to print two cubes that were placed in either a solution of $CaSO_4$ dissolved in ethanol or $CaCl_2$ dissolved in H_2O. This was done to test if SA would ionically crosslink further when submerged in a solution with high calcium content. Two calcium compounds were used in the solutions to determine if they yielded different results. The first cube ($CaSO_4$ in ethanol) reticulated quickly but shrunk considerably despite maintaining its original shape and was fragile (breakable). The second cube did not reticulate as fast as the first but its corners became rounder, changing the original shape completely, figure 4.4.

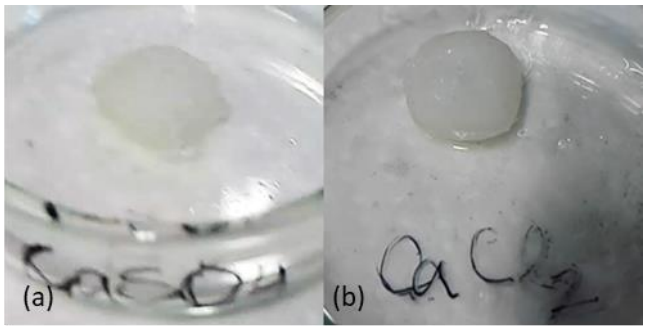

Figure 4. 4 - 3D Printed cubes of sample 14 after being submerged in (a) $CaSO_4$ or (b) $CaCl_2$

4.2.2 Polymer mixture B

Polymer mixtures B and A are similar but B2VT replaces the BAPO (**PEGDA, B2VT, SA, and $CaSO_4$**). The use of BAPO aimed to demonstrate that it was possible to print the polymer mixture. The goal was to change the photoinitiator BAPO, since it is not soluble in water, unlike all the other components. BAPO was used until Riboflavin and TEOHA were available in the laboratory. The first solutions made with these mixtures were hand printed but deemed too liquid except for the composition of C5 as in figure 4.5. Different amounts of $CaSO_4$ were tested in the mixture and a decrease in the mixture's uniformity with the increase of $CaSO_4$ was detected, probably due to its low solubility in water. Five different sets of samples were tested with different concentrations of the new photoinitiator B2VT (table 4.2).

Table 4. 2 – Polymer mixture B; Parameters varied with PEGDA 34.78% (2.25mL); SA (5%)

Sample	$CaSO_4$ + 0.75 mL H_2O (B2VT: 0.15 mL)	Sample	$CaSO_4$ + 0.75 mL H_2O (B2VT: 0.3 mL)
C1A	8.1 mg	**C2A**	8.1 mg
C1B	6.6 mg	**C2B**	6.6 mg
C1C	5.1 mg	**C2C**	5.1 mg
C1D	3.6 mg	**C2D**	3.6 mg

Sample	$CaSO_4$ + 0.75 mL H_2O (B2VT: 0.45 mL)	Sample	$CaSO_4$ + 0.75 mL H_2O (B2VT: 0.6 mL)	Sample	$CaSO_4$ + 0.75 mL H_2O (B2VT: 0.75 mL)
C3A	8.1 mg	**C4A**	8.1 mg	**C5A**	8.1 mg
C3B	6.6 mg	**C4B**	6.6 mg	**C5B**	6.6 mg
C3C	5.1 mg	**C4C**	5.1 mg	**C5C**	5.1 mg
C3D	3.6 mg	**C4D**	3.6 mg	**C5D**	3.6 mg

Figure 4. 5 – Handprinted samples C1A, C2A. C3A, C4A, and C5A before (A) and after (B) UV reticulation

First tests with the 3D plotter were performed and as the UV laser effect on the reticulation of polymer mixture B was unknown, preliminary trials with different numbers of printed layers were done. Control pieces were printed with 1, 2, 3 and 4 layers to determine the effect of UV reticulation and test the material's printing - figure 4.6. Further improvements were tested by refining the ratio between components as seen in table 4.3.

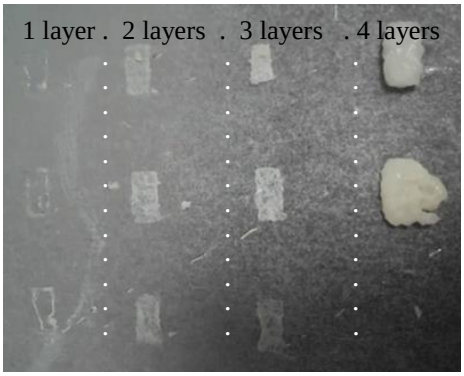

Figure 4. 6 – 3D printed and UV reticulated C5 samples printed with 1, 2, 3 and 4 layers

Table 4. 3 – Polymer mixture B, change of components ratio ($CaSO_4$+H2O (mL): 0.0108 g + 1)

Sample	PEGDA 34.78%	B2VT	SA 5%
C5A1	3 mL	1 mL	3 mL
C5A2	2.5 mL	1 mL	2.5 mL
C5A3	2.5 mL	0.5 mL	2.5 mL

Although C5A composition was the best for printing (figure 4.5) the paste was too liquid and needed to rest for hours before being ready to print. We tried lowering the percentage of water so the paste was ready to print sooner (C5A2) and prolonging the usage time of the paste by lessening the percentage of photoinitiator (C5A3). One of the issues faced was what laser power to use during printing, being the maximum 3.8 W. The power of laser should be high enough to start reticulating each layer but not so high as to prevent different layers from forming one cohesive film or burning.

4.2.3 3D printing of samples

Samples were first printed and reticulated with UV laser from 1 to 100 to determine the minimum power needed to maintain the shape printed as well as the maximum value before burning the hydrogel, as described at the end of section 3.2. It was found that only samples from 15 forward had the desired consistency but only samples from 30 forward kept the printed shape after drying. The cubes used to perform compression tests were, therefore, reticulated with laser power corresponding from 30 to 100. These cubes were labelled according to their G-code reference and sample number – for example, AC302 stands for Alginate Compression, G-code reference 30 (corresponding to 471 mW) and sample number 2. No tests were made for the first sample of each reference because their infill density was too low and created a non-homogenous

material. Samples AC70 and AC90 were not tested since the results from other samples provided enough data to infer their behaviour. Figure 4.7 shows samples printed for mechanical testing.

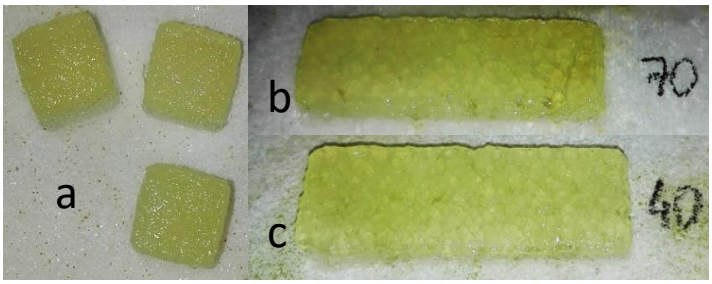

Figure 4. 7 – Examples of printed samples for (a) compression testing (10 x 10 x 10 mm) and (b)(c) tensile testing (10 x 30 x 2 mm)

All samples printed reduced in size continuously for a few days. This happens due to the hydrogels' water content, some part of which evaporates, leaving the sample smaller and more brittle. Cubic samples printed for compression testing were measured after a minimum of 120 hours and were found to have in average: 64 % (± 2 %) of the original thickness, 72 % (± 4 %) of the original length, 71 % (± 3 %) of the original width, and 33 % (± 4 %) of the original volume. A total of 33 samples were measured: four for each laser power and an extra for the laser power corresponding to 60.

The 3D printing of tracheal sections was done as described in section 3.2 and led to objects such as those shown in figure 4.8. These were malleable but slightly fragile when folded into themselves. Several samples were printed with different wall thicknesses and it was found that, while small sections of the sample became less fragile with increased thickness, the overall object became too difficult to fold, which hindered the original goal of an easy implantation process. It was also found that, if the sample was handled and rolled frequently during the drying process, it would become less prone to break when folded after drying.

Unfortunately, and unlike what was expected, this material started to quickly break into pieces and dissolve when placed in water or simulated body fluid (SBF), meaning that it cannot be used on its own for prostheses, requiring at least some kind of hydrophobic coating.

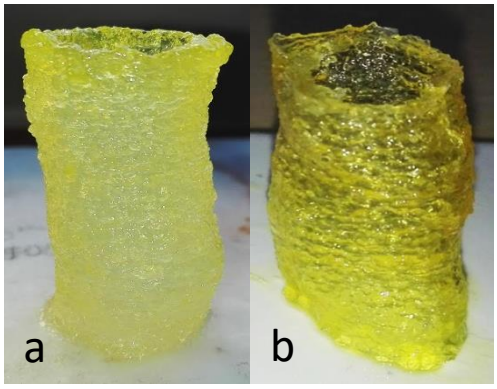

Figure 4. 8 - Tracheal section 3D printed with simultaneous UV reticulation: (a) right after printing (height = 38.5 mm, width = 19.24 mm, thickness = 0.5 mm) and (b) after 72 hours

Several tests were done with the purpose of finding a solution for this problem, involving the addition of other polymers such as PS or PVP (Polyvinylpyrrolidone) in the printed mixture or a PVA coating after printing. Some of these possible solutions were not adequate as they involved toxic solvents that would be very difficult to remove from the final product. The PVA coating was applied by completely covering the sample in a PVA solution, while under vacuum, so the space occupied by air could be filled with PVA, which would stop the object's dissolution in water. The most viable solution seems to be a PVA coating done not immediately after printing (figure 4.9) since the object tested suffered some swelling, nor when the object has finished shrinking, but sometime in between. This could mean that a solution with higher PVA concentration is needed or that we would need to wait longer before starting the coating process. More tests are needed in this regard.

Figure 4. 9 – Tracheal section 3D printed and immediately coated with PVA

4.2.4 Polymer Mixture C

The mixture C and A are similar, being the sodium alginate (SA) and Calcium ($CaSO_4$) replaced by PVA (**PEGDA, BAPO, PVA**). The goal was to test the influence of PVA to enhance the consistency of paste.

The samples were made mixing 2 mL PEGDA at 28.75% v/v with 1mL of PVA at 20% w/v and various concentrations of BAPO (1.5 %) and $CaCl_2$ or $CaSO_4$ as shown in table 4.4.

Table 4. 4 - Composition of Polymeric Mixtures C

Sample	PEGDA (28.75 % v/v)	$CaCl_2$ (0.07 M)	$CaSO_4$ (0.07 M)	BAPO (1.5 %)	PVA (20 % w/v)
21A	2 mL	150 µL	-	-	1 mL
21AA	2 mL	150 µL	-	150 µL	1 mL
21B	2 mL	-	150 µL	-	1 mL
21BA	2 mL	-	150 µL	150 µL	1 mL
21C	2 mL	-	-	0.01 g	1 mL
21D	2 mL	-	-	0.03 g	2 mL
21CB	2 mL	-	-	0.055 g	1.5 mL
21CD	2 mL	-	-	0.045 g	1 mL
21CC1	2 mL	-	-	0.15 g	2 mL
21CC2	2.5 mL	-	-	0.15 g	2 mL

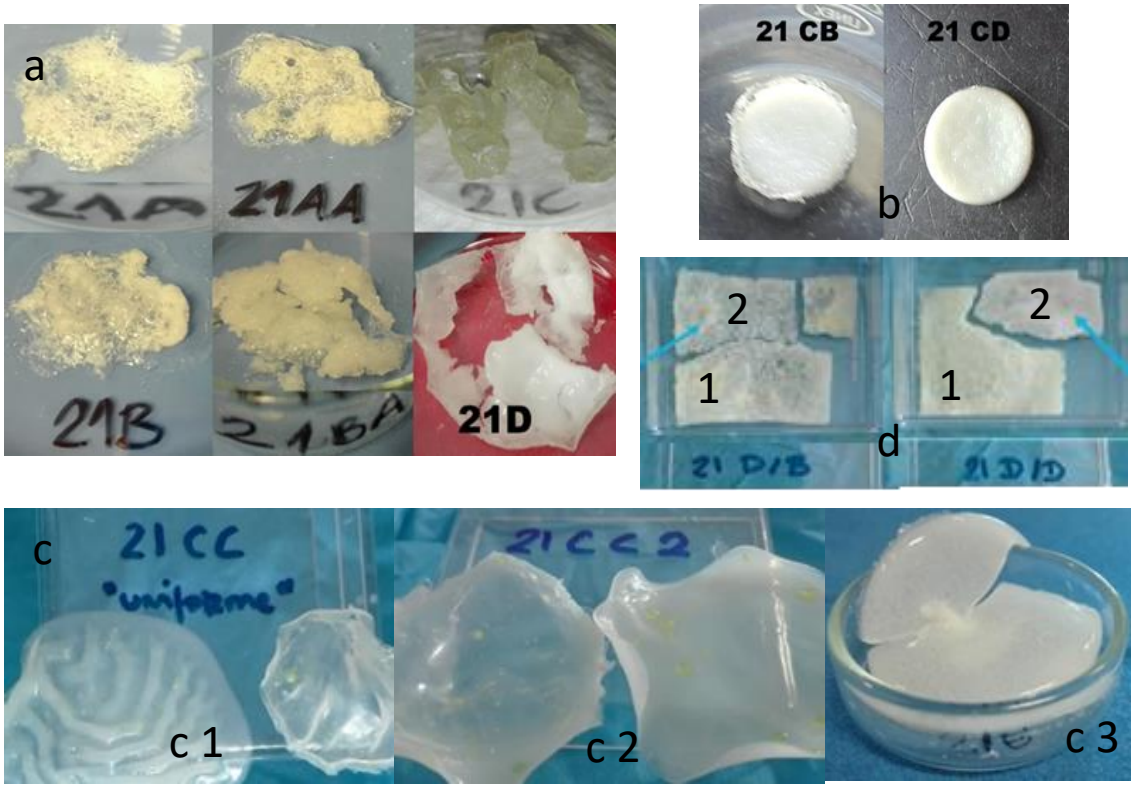

Figure 3. 7 – a) PVA based samples after UV reticulation; b) Reticulated pellets of 21CB and 21 CD mixtures; c) Reticulated films of (c1) 21 CC 1; (c2) 21 CC 2 and (c3) 21E; d) Reticulated Films of 21 DD and 21 DB (1) before and (2) after being submerged in PBS

Photographs of prepared samples are shown in figure 3.7 after UV reticulation. The samples 21A to 21C look like foam and are too viscous (figure 3.7 (a)). Samples, where $CaCl_2$ is used, retain more water than those with $CaSO_4$. Pellets were made with 21CB and 21CD compositions, as shown in figure 3.7 (b). Sample 21 CC2 shows more elasticity than 21E, bending 180 º without breaking and returning to its original shape.

Sample 21 E has 2 mL of 30 % PVA w/v, 0.15 g of BAPO and 2 mL of PEGDA 28.57% v/v. It became more fragile than previous samples with less percentage of PVA probably because it was exposed to light and air before being reticulated under UV light. The fault lines can be observed in figure 3.7 (c3).

Both 21 DB and 21 DD samples were very porous and dry but still malleable, as can be seen in figure 3.7 (d). They were submerged in PBS (Phosphate Buffered Saline) and left to dry for four days. The samples returned to their original size and maintained their shape and malleability while becoming slightly more fragile

4.2.5 Polymer Mixture D

Polymer mixtures D and C are similar but B2VT replaces the BAPO (**PEGDA, B2VT, and PVA**). The photoinitiator was replaced as described in section 4.2.2.

Refinement of the previous study was performed according to table 4.5, using 2 mL of PEGDA (34.78 % v/v).

Table 4. 5 – Composition of Polymeric Mixtures D: 2 mL PEGDA (34.78 % v/v).

Sample	PVA 25%	B2VT	Sample	PVA 15%	B2VT	Sample	PVA 5%	B2VT
D3A	2 mL	0.3 mL	**D3B**	2 mL	0.3 mL	**D3C**	2 mL	0.3 mL
D4A	2 mL	0.4 mL	**D4B**	2 mL	0.4 mL	**D4C**	2 mL	0.4 mL
D5A	2 mL	0.5 mL	**D5B**	2 mL	0.5 mL	**D5C**	2 mL	0.5 mL

Figure 4. 10 – Samples D5A (thickness of 1 mm); D5B (thickness of 7.5 mm), and D5C (thickness of 4 mm) after UV reticulation

Three different concentrations of PVA were tested, each with different amounts of B2VT. To achieve a mixture that reticulates well under UV light, the ingredients must be mixed together at a temperature of approximately 80ºC and maintained at that temperature for the initial stages of reticulation to avoid deposition. The temperatures' effect is particularly well displayed in figure 4.10, where the increase in thickness (volume deposited in the mould) is shown to correlate with an increase in layer differentiation. These results are not dependant on the sample used but instead, are replicated independently of PVA percentage. There is also a possibility of printing the same mixture in the SLA (Stereolithography) printer, but we believe the same differentiation issue would occur.

The result of trying to create a sample thick enough to undergo compressive testing was a two-layered film with a fragile white layer and a flexible yellow layer as can be seen in figure 4.10 (D5C), which shows samples with different thicknesses. This tells us that the UV rays could not penetrate deep enough before deposition occurred. It was determined that compression tests were to be made despite it a non-homogenous film. The decision was that only on the already reticulated D5C samples would undergo compressive testing. The films for tensile testing were reticulated in a squared transparent plastic box and then cut into rectangles with 10 x 30 mm and did not dissolve in water, unlike the material from mixture B. Being hydrogels, like the material in samples of polymeric mixture B, the samples shrink when reticulating and continue shrinking afterwards.

4.3 Mechanical properties Tests

Young's Modulus (*E*); Maximum Stress; Maximum Strain; Maximum Force and Initial Distance between claws are presented for each Tensile test. In addition, the Average value and standard deviation (STD) for each type of sample are also presented, as is an Average* and respective STD* when outlier values were removed.

The strain-stress curves for each D sample are shown in Annexe A. Table 4.6 shows the obtained average values from a set of at least 5 measurements. Examples of traction stress-strain curves are shown in figures 4.11 and 4.12. Figure 4.11 shows the influence of B2VT percentage for 5% PVA, where elongation of about 60 % is observed at a lower B2VT percentage. As B2VT increases to 0.5 mL, the elongation before the break is reduced to about 30 %. A B2VT

quantity of 0.5 mL seems to enhance the rigidity of samples, which is possibly related to a more efficient reticulation of PEGDA.

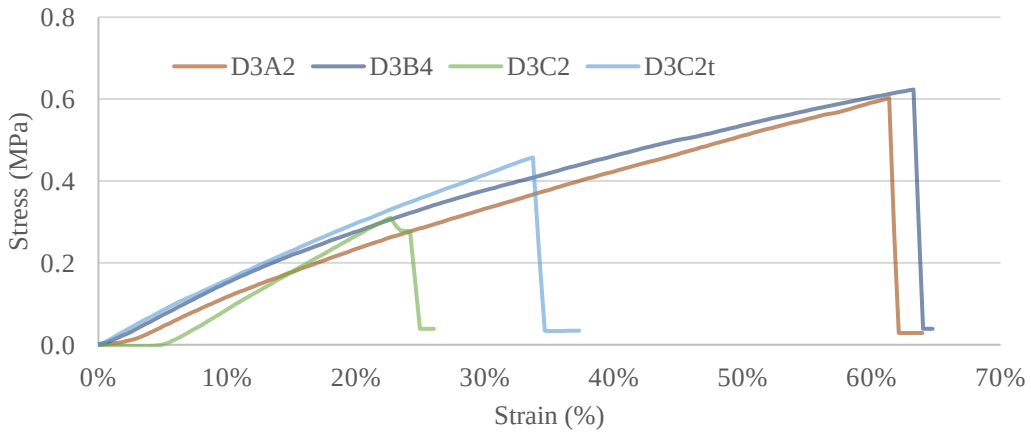

Figure 4. 11 – Examples of D3 Stress-Strain Curves – Traction

The influence of PVA on the strain-stress curves is highlighted in figure 4.12 where we can clearly see that both elongation and maximum stress are promoted by the increase in PVA percentage, as expected. However, there is a great variation between samples, possibly due to a non-uniform UV crosslink in the interior of the polymeric object.

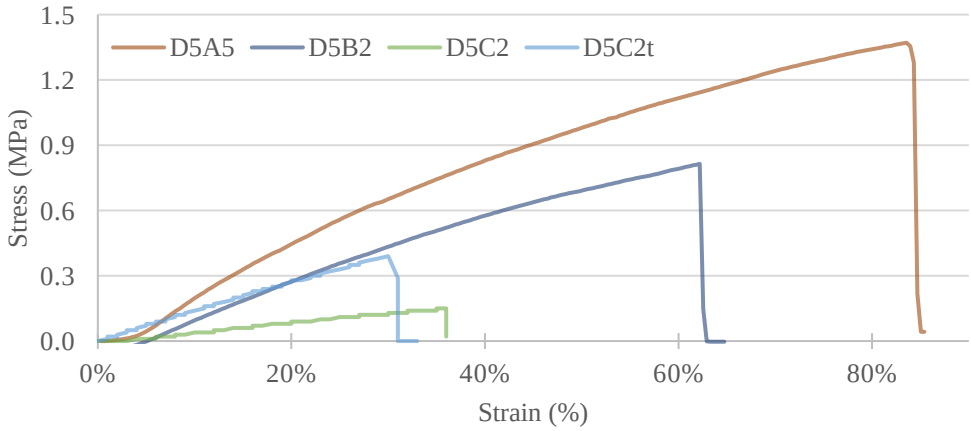

Figure 4. 12 – Examples of D5 Stress-Strain Curves – Traction

The average mechanical properties of D samples are compiled in table 4.6. We can see a stable Young's Modulus and Maximum Stress with 0.3 mL of B2VT, despite the decrease in overall PVA percentage (A = 25 %; B = 15 %; C = 5 %). There is a decrease in Maximum Strain associated with the decrease in PVA percentage. This behaviour is also observed for D4 and D5 samples despite the increase in B2VT.

Table 4. 6 - Average Mechanical Properties of D samples

Sample	Young's Modulus (MPa)	Max Stress (MPa)	Max Strain (%)	Max Force (kg)	Initial Distance (mm)	Variation PVA | B2VT	
D3A	2.43	0.62	57%	0.65	12.3	25%	0.3 mL
D3B	2.70	0.66	51%	0.67	12.3	15%	
D3C	1.41	0.44	27%	0.48	12.3	5%	
D3Ct	2.40	0.61	32%	0.32	10		
D4A	2.32	0.49	80%	0.47	12.3	25%	0.4 mL
D4B	2.94	0.71	49%	0.59	12.3	15%	
D4C	1.43	0.28	32%	0.28	12.3	5%	
D4Ct	3.09	0.64	60%	0.42	10		
D5A	4.55	1.13	75%	1.05	12.3	25%	0.5 mL
D5B	3.24	0.89	65%	0.79	12.3	15%	
D5C	0.78	0.11	30%	0.11	12.3	5%	
D5Ct	1.97	0.31	35%	0.21	10		

There is an accentuated decrease in Maximum Strain correlating with the decrease in PVA percentage if we disregard sample D4Ct. Smaller samples (t) seem to give significantly higher results in all properties than longer samples made under the same conditions.

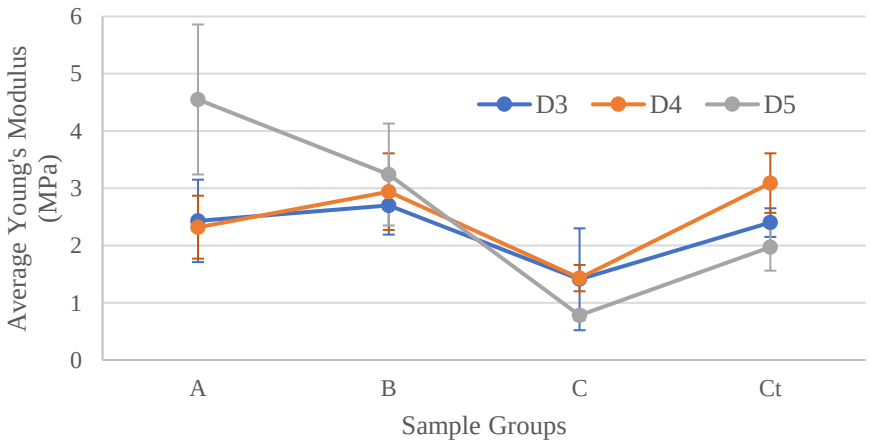

Figure 4. 13 - Average Young's Modulus (MPa) for D Samples - Traction

A variation of Young's Modulus is depicted in figure 4.15. The average values and the errors displayed show that sample C is the one with lower *E* values while the values for samples

A, B and Ct are similar and higher. However, sample D5A has a much higher Youngs' Modulus than other A samples.

For samples D3 and D4, *E* increases slightly when the PVA solution lowers to 15 % but decreases again at 5 % PVA. One possible explanation for this is that the difference between using a 25 % or 15 % PVA solution is only significant with a higher volume of photoinitiator. For lower volumes of B2VT, only a low percentage PVA solution (5 %) manages to lower Young's Modulus value and still creates no statistically significant difference between D3 and D4 samples. On the other hand, even a higher volume of photoinitiator cannot reticulate enough PEGDA to increase or even maintain a higher *E* with a 5 % PVA solution. As expected, a higher volume of photoinitiator associated with a higher percentage of PVA increases the material's Young's Modulus.

Compared to the same samples tested less than 48h after they were reticulated (C samples), those tested a week after they were reticulated (Ct samples) present a higher E in every case. This could be due to the loss of water during that time, leading to a stronger and more flexible membrane.

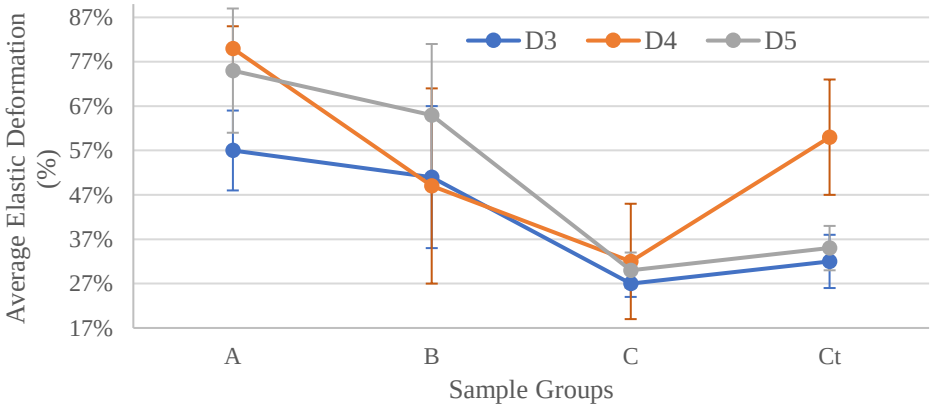

Figure 4. 14 - Average Elastic Deformation (%) of D Samples – Traction

The average Elastic Deformation or Strain for each membrane type is represented in figure 4.14. Considering an average between C and Ct values, the average Strain decreases continuously with the decrease of PVA. This appears in agreement with what was presented before, that an increase in PVA percentage reinforces the membrane. The values obtained also indicate that higher volumes of photoinitiator give more flexibility to the membrane. The maximum strain is obtained for samples with the highest percentage of PVA as expected due to the plasticizer effect of PVA.

4.4 Compression Tests

Perpendicular and Parallel compression tests were done in samples reticulated with each different laser power, as specified in sections 3.2 and 3.3. The stress-strain curves obtained are

shown in Annexe B, as well as the corresponding values for Young's modulus and Maximum Stress. The dimensions of each sample were measured three times using a digital Vernier calliper and the average value was recorded. The measurements were performed before and after compression. The compression tests were done parallel and perpendicularly to the printing lines.

4.4.1 Samples of polymeric mixture B

Each table comparing the results between Parallel and Perpendicular tests shows the average values and STD for the Maximum Applied Force in kg, Maximum Stress in MPa and the Young's Modulus for both slopes showed in the corresponding graphics. The value of each slope was calculated with a linear fit to the curve in question. After analysing the data, it was concluded that only the first slope corresponds to the Young's Modulus of the material tested due to high STD values for the second slope.

The stress-strain curves obtained are shown in Annex B. Figure 4.15 shows the curves for one of the tested conditions, UV laser 941mW. The stress-strain curves show a typical polymer foam behaviour: a first elastic regime where the Young's Modulus was calculated, then a plastic plateau corresponding to absorbing energy by compression of polymer molecules and finally the ultimate densification and rupture of the polymer chain bonds. We calculate the maximum stress Before the break.

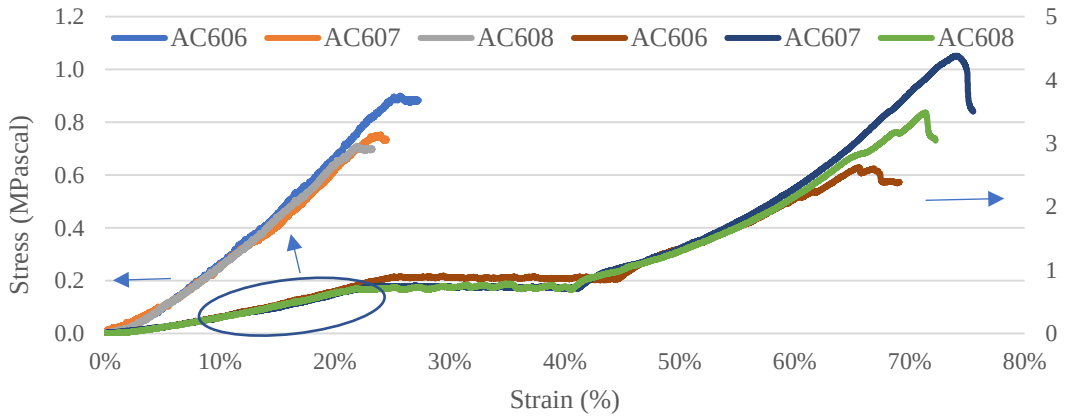

Figure 4. 15 - Stress-Strain Curves for Parallel Compression Tests of Cubes Reticulated at 941 mW – first slope for each curve on the left axis and original curve for each sample on the right axis

Table 4.7 - Comparing the Average Values of Young's Modulus for Parallel and Perpendicular Compression Tests for cubes reticulated with UV laser at different powers.

Laser Power (mW)	Sample	Meas. Direct.	Max Stress (MPa)	Max Force (Kg)	Young's Modulus (MPa)	Slope 2 (MPa)
470	AC30	‖	3.46 ± 0.45	11.43 ± 1.3	5.71 ± 2.3	39.91 ± 8.7
		⊥	5.45 ± 2.1	26.29 ± 10	4.64 ± 1.9	106.74 ± 38
627	AC40	‖	5.33 ± 1.8	17.09 ± 3.3	5.76 ± 2.1	81.50 ± 40
		⊥	6.93 ± 1.0	27.08 ± 5.5	6.99 ± 1.5	101.88 ± 21
784	AC50	‖	3.20 ± 0.32	9.88 ± 1.5	6.72 ± 0.63	37.41 ± 6.7
		⊥	7.08 ± 1.1	24.16 ± 2.7	5.98 ± 0.88	115.63 ± 24
941	AC60	‖	3.49 ± 0.88	11.33 ± 3.6	6.87 ± 0.72	40.50 ± 12
		⊥	9.45 ± 2.5	35.16 ± 8.1	6.72 ± 1.4	177.87 ± 62
1255	AC80	‖	4.31 ± 0.97	13.02 ± 3.2	6.66 ± 0.92	46.18 ± 13
		⊥	5.05 ± 1.0	23.82 ± 6.7	6.09 ± 1.1	74.15 ± 24
1569	AC100	‖	3.31 ± 1.1	11.68 ± 4.9	6.29 ± 0.44	45.52 ± 17
		⊥	2.52 ± 0.48	14.42 ± 1.8	5.45 ± 1.2	28.35 ± 4.8

The following graphs give a comprehensive visualisation of the effect of UV laser power on the mechanical properties of samples.

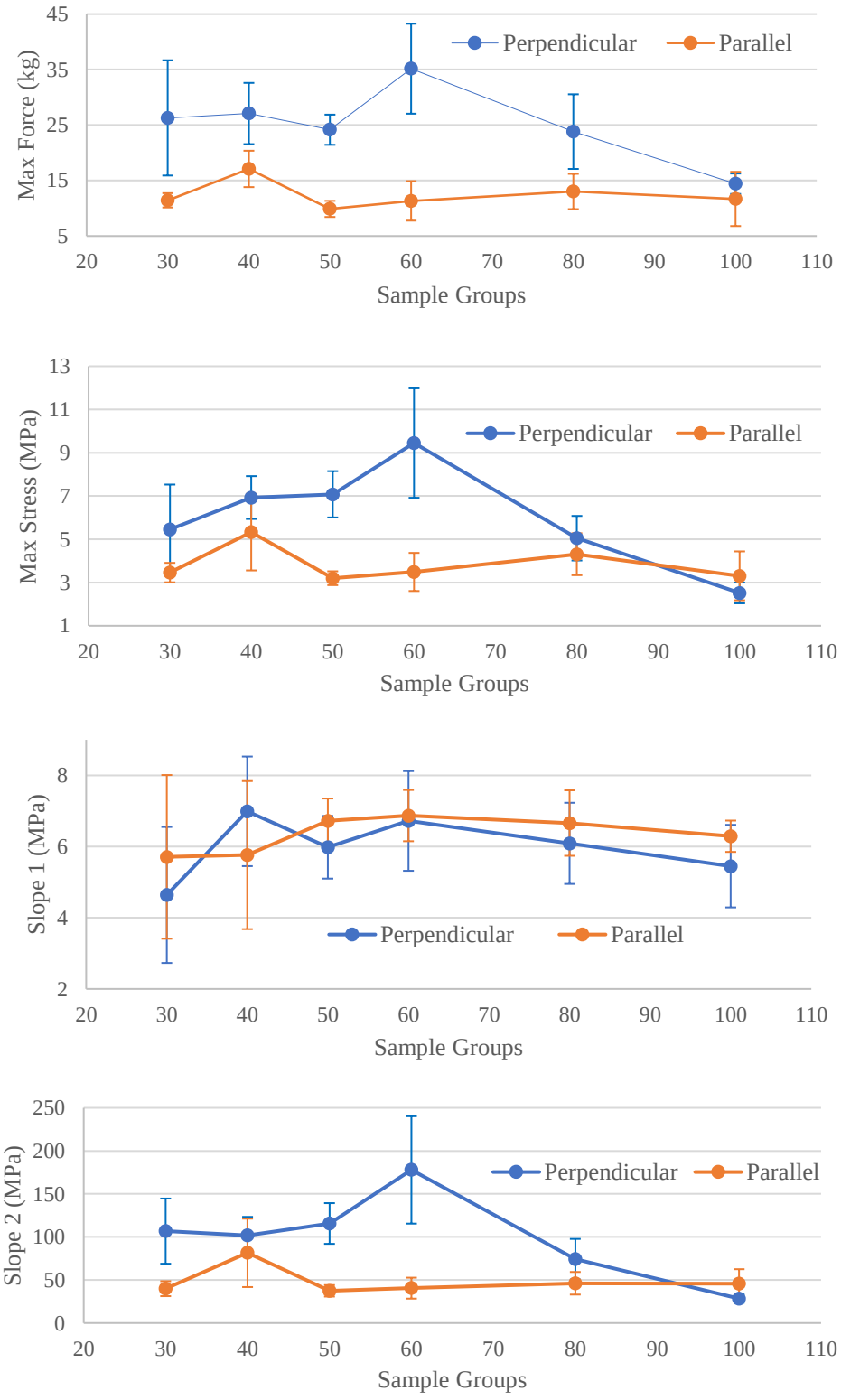

Figure 4. 16 – Variation of: a) Maximum Force (kg), b) Maximum Stress (MPa), c) Young's Modulus (MPa) and d) Second Slope (MP) for Parallel and Perpendicular Compression Tests for all cubes reticulated with UV laser

The average values of maximum applied force (kg) and maximum stress (MPa) for parallel compression tests are significantly lower for each reticulation value than for perpendicular compression, with an exception for group 100, as shown in table 4.7. The average values of Young's Modulus (MPa) for parallel compression tests are similar for all samples considering the standard deviation (STD). As observed by the graphs of figure 4.16, the maximum applied force, the maximum stress and the slope 2 have all the same trend for the set of samples analysed, showing their correlation.

The average values of the second slope (MPa) for parallel compression tests differ completely from those for perpendicular compression, for each reticulation value, as shown in table 4.7. The significance of these values, particularly for sample groups 30, 50, and 60 is demonstrated by the STD bands for each compression type – figure 4.16.

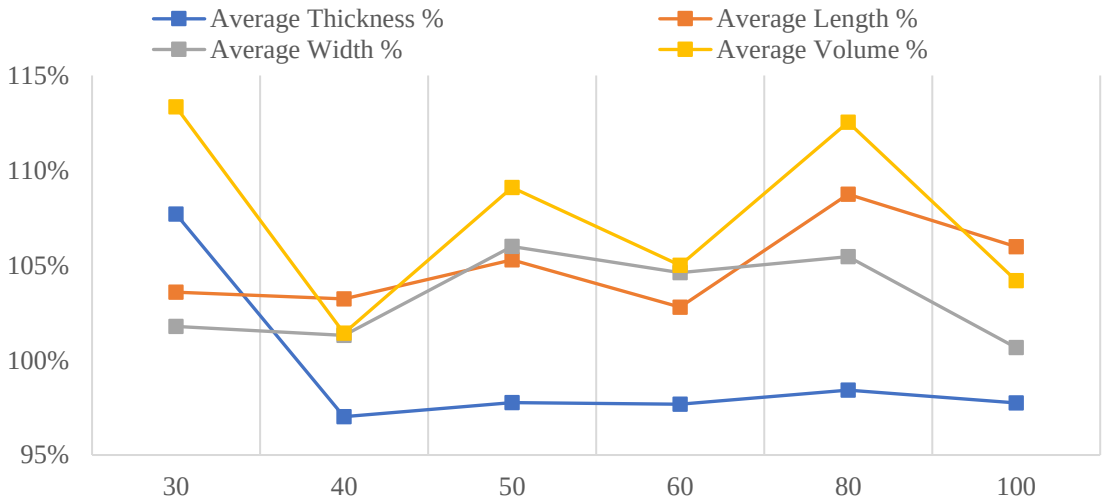

Figure 4. 17 - Average Measurements After Perpendicular Compression (%) of each sample type

The average measurements in thickness, length, width and volume after perpendicular compression for each sample type are represented in figure 4.17. Here we can see a 10 % decrease in thickness for reticulations higher than 30. In general, the original shape of the samples is maintained.

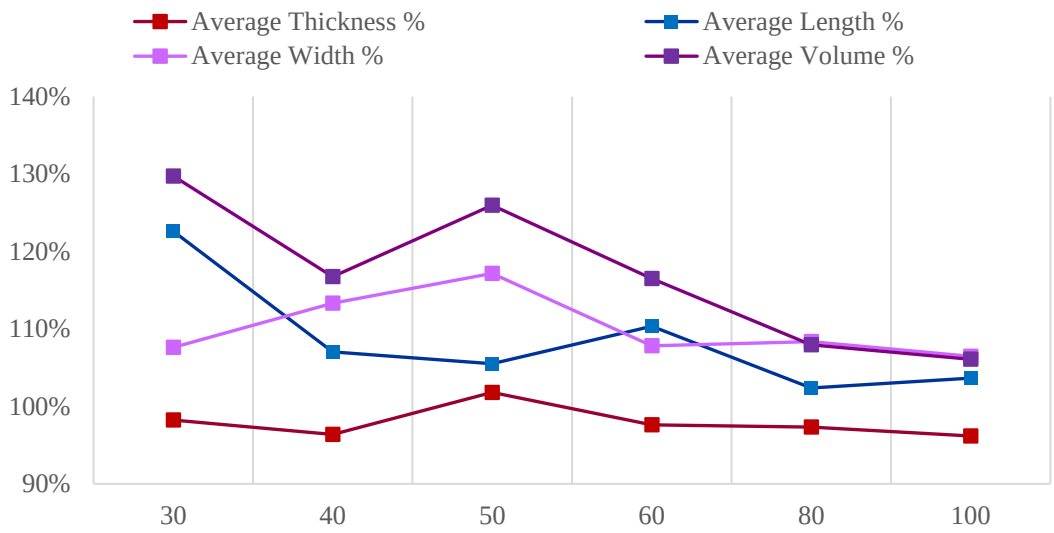

Figure 4. 18 - Average Measurements After Parallel Compression (%) of each sample type

The average measurements in thickness, length, width and volume after parallel compression for each sample type are represented in figure 4.18. Here we can see a 10 % decrease in length for reticulations higher than 30. Thickness measurements appear stable for all reticulation values. In general, the original shape of the samples is maintained.

4.4.2 Samples of polymeric mixture D

Young's Modulus (E); Stress (σ); Strain (ε); Maximum Applied Force and Initial Distance between claws are presented for each Compression test, in addition, the average value and standard deviation (STD) for each type of sample are also presented.

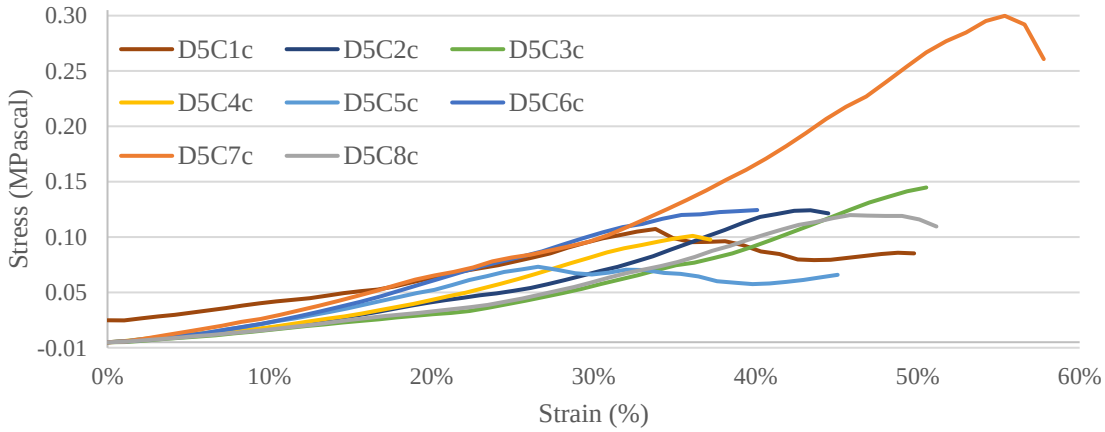

Figure 4. 19 - D5Cc Stress-Strain Curves - Compression

The stress-strain curves of D5Cc membranes are represented in figure 4.19 and the corresponding mechanical properties are represented in table 4.8. In average, Young's Modulus for these membranes is of 0.91 (± 0.24) MPa and the Maximum Stress is of 0.11 (± 0.02) MPa.

Table 4. 8 - Mechanical Properties of each D5Cc sample

Sample	Young's Modulus (MPa)	Max Stress (MPa)	Max Strain (%)	Max Force (kg)	Initial Distance (mm)
D5C1c	0.74	0.10	34%	1.36	4.41
D5C2c	1.13	0.12	43%	1.61	4.41
D5C3c	1.31	0.14	51%	2.06	4.10
D5C4c	0.78	0.10	36%	1.38	4.40
D5C5c	0.61	0.07	27%	0.94	4.38
D5C6c	0.86	0.12	40%	1.77	3.90
D5C7c	2.49	0.29	55%	1.38	3.84
D5C8c	0.95	0.11	47%	1.53	4.23
Average	0.90	0.13	42%	1.50	4.21
STD	0.26	0.07	9%	0.36	0.22
Average*	0.91	0.11	43%	1.52	4.20
STD*	0.24	0.02	7%	0.35	0.24

It is apparent in curves D5C1/2/7/8 the existence of two different regimes during compression. First, we have a phase where the air is compressed out of the hydrogel's pores, needing less applied tension to produce about 25 % deformation – elastic zone. Then, after the pores have been closed, another regime begins where more tension is required to deform the hydrogel until it reaches its breaking point.

It is important to remember that these samples were not completely homogeneous since the UV rays could not penetrate the hydrogel completely before deposition occurred as shown in figure 4.20.

Figure 4. 20 - D5Cc samples with two phases after UV reticulation

4.5 FTIR

The FTIR spectra (Absorbance) of DLLA, TMC, and PLMC are shown in figure 4.21.

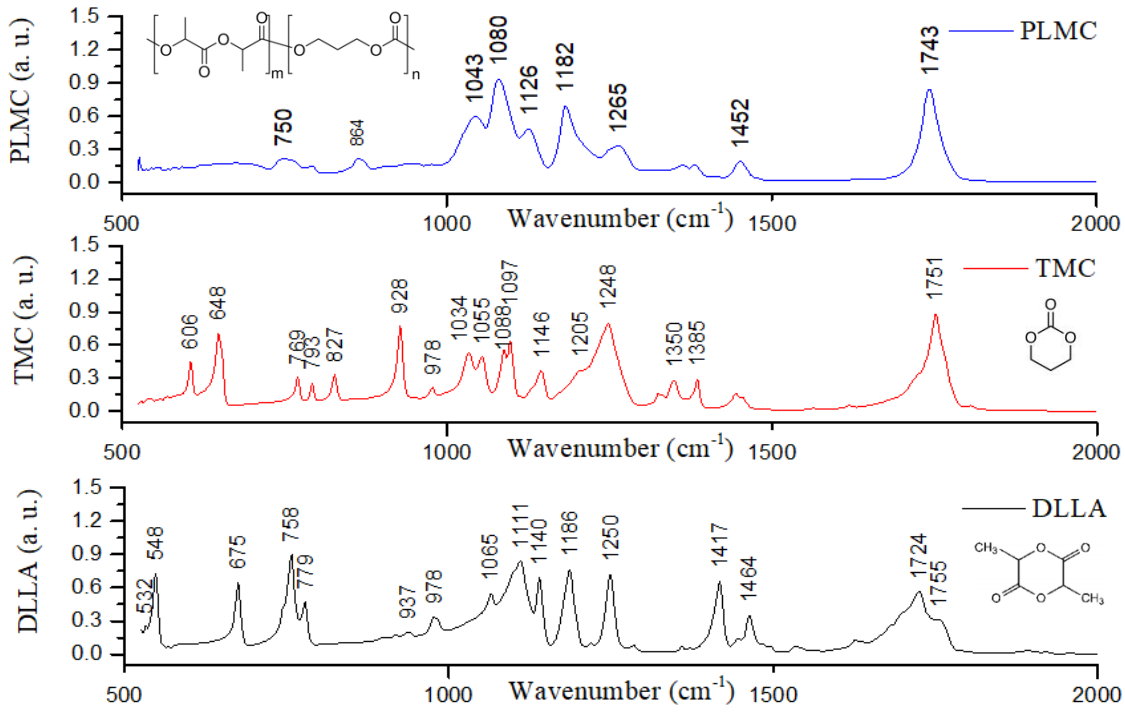

Figure 4. 21 - FTIR spectra of DLLA, TMC, and PLMC

The characteristic vibration bands of TMC occur at 1751 cm^{-1} (C=O) and 1248 cm^{-1} (O-C-O asymmetrical stretching) and shift to 1743 cm^{-1} and 1265 cm^{-1} respectively in the PLMC spectra. The bands corresponding to DLLA occur at 1724 cm^{-1} and 1755 cm^{-1} (C=O) and 1186 cm^{-1} (C-O-C) and shift to 1452 cm^{-1} and 1182 cm^{-1} respectively in the PLMC spectra [38].

The FTIR spectra (Absorbance) of PVA, BAPO and PEGDA/BAPO/PVA are shown in figure 4.22.

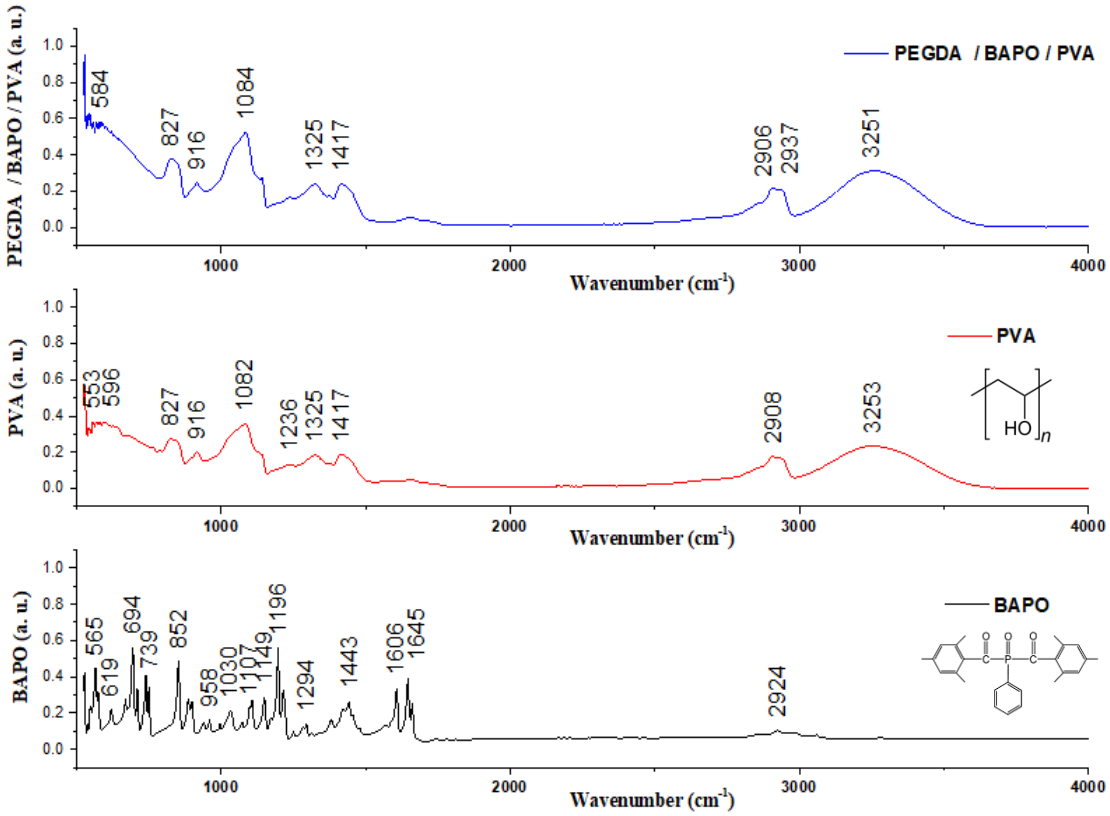

Figure 4. 22 - FTIR spectra of PVA, BAPO and PEGDA/ BAPO/PVA

The vibration bands attributed to PVA are observed at 3253 cm^{-1} (OH stretching), 2908 cm^{-1} (–CH stretching), 1417 cm^{-1} (–CH bending), 1325 cm^{-1} (CH + OH bending), 1082 cm^{-1} (CO stretching), and 827 cm^{-1} (C-C stretching) due to acetate groups which are still present in the partially hydrolysed form of PVA [39][40]. These same peaks appear in the mixture of PEGDA/ BAPO/ PVA with an added peak at 584 cm^{-1} (aromatic C-H bending) probably due to the aromatic rings in BAPO.

4.6 UV-Vis Spectrophotometry

Regarding the UV-Vis absorption spectra of the PEGDA, a very well-defined absorption band is visible at lower wavelengths, presenting a maximum at around 230 nm. The mixture including SA and PEGDA showed no differences in UV absorption when compared with the samples containing just PEGDA, presenting a similar band with a maximum at around 230 nm (figure 4.23).

On the other hand, the mixture of PEGDA and B2VT reached a saturation amount of absorption along the previously mentioned band, slightly shifting it so 260 nm. Along with this band, two others are visible, with maximum values at 450 nm and 360 nm, although with much smaller absorption percentage values. The mixture of PEGDA, B2VT, and SA showed almost no variations when compared to the mixture of PEGDA and B2VT, maintaining the same bands and wavelength values for each maximum, although an additional UV absorption band is now visible reaching saturation values of absorption while centred around 215 nm (figure 4.24).

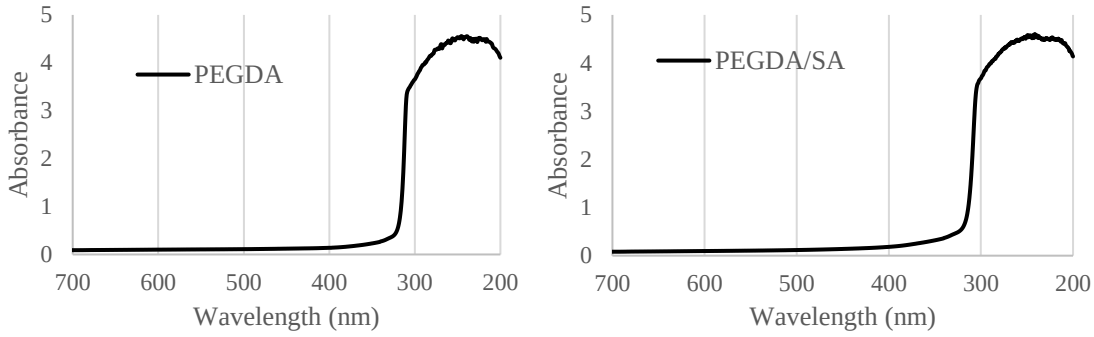

Figure 4. 23 - UV-Vis Absorption Spectra for PEGDA and for the mixture PEGDA / SA

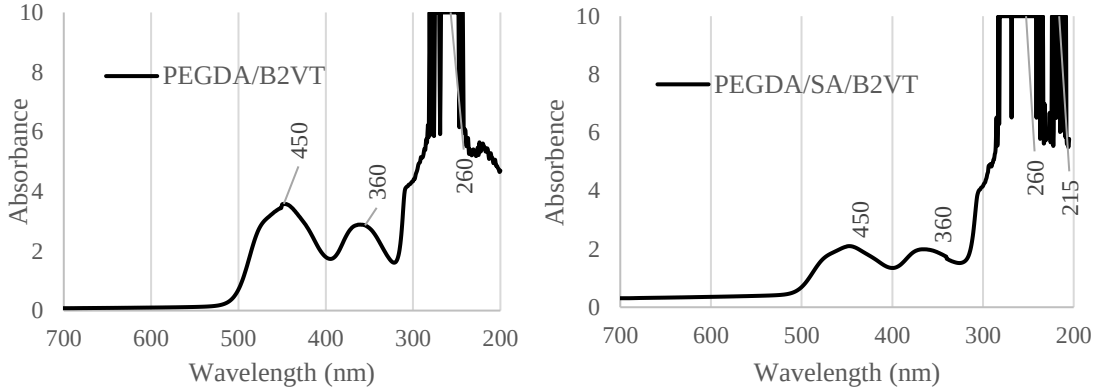

Figure 4. 24 - UV-Vis Absorption Spectra for the mixtures PEGDA/B2VT and PEGDA/SA/B2VT

4.7 Cytotoxicity

As shown in section 3.6, the chosen method of testing a material's cytotoxicity is based on cell viability while in a medium conditioned by said material. According to the adopted classification for extraction tests, the materials were classified as non-cytotoxic if relative cell viability (RCV) is greater than 80 %; slightly cytotoxic is RCV is between 80 % and 60 %; moderately cytotoxic it RCV is between 59 % and 40 %, and fatal if RCV is lower than 40 %.

In the first test, samples C5B and D5A were extracted at a 15 % w/v ratio. These were then diluted to achieve w/v ratios of 10 % and 5 %. The relative cellular viability for this test is represented in figure 4.25. Values for the negative control (NegC) and positive control (PosC) at 10 % of DMSO are also shown.

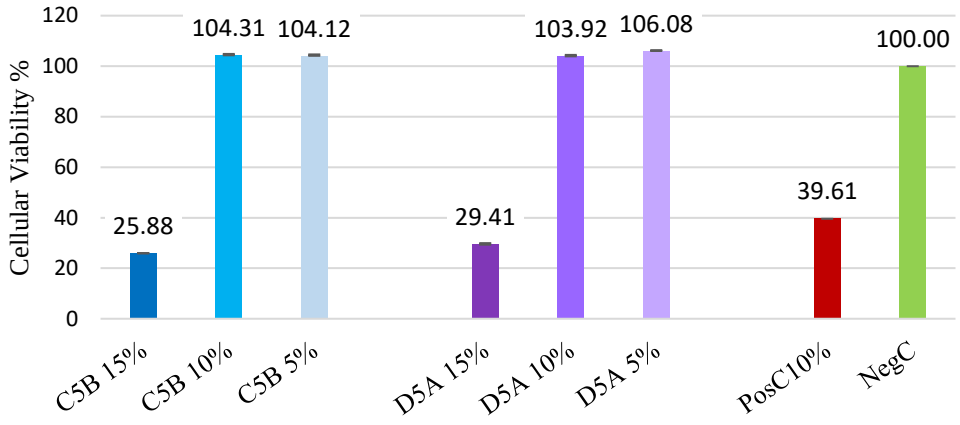

Figure 4.25 - Relative Cell Viability of Samples C5B and D5A

It was found that, for both samples, concentrations of 15 % were fatal while those lower were non-cytotoxic. Considering the materials are hydrogels it was hypothesized that ethanol was absorbed in the process of sterilization and did not evaporate, causing increased toxicity. This was assumed because there is no cell toxicity recorded for the common components of samples C and D which are PEGDA, Riboflavin, and Triethanolamine when used in these ratios.

To test this hypothesis, a second cytotoxicity test was done. This time samples were sub-merged in ethanol for only 5 minutes. The rest of the sterilization procedure was the same. The samples used were C5A and D5B, which were extracted at a 20 % w/v ratio. These were then diluted to achieve w/v ratios of 15 %, 10 %, and 5 %. The relative cellular viability for this test is represented in figure 4.26. Relative values are also shown for the negative control (NegC) and positive control (PosC) at 10 % and 20 % of DMSO.

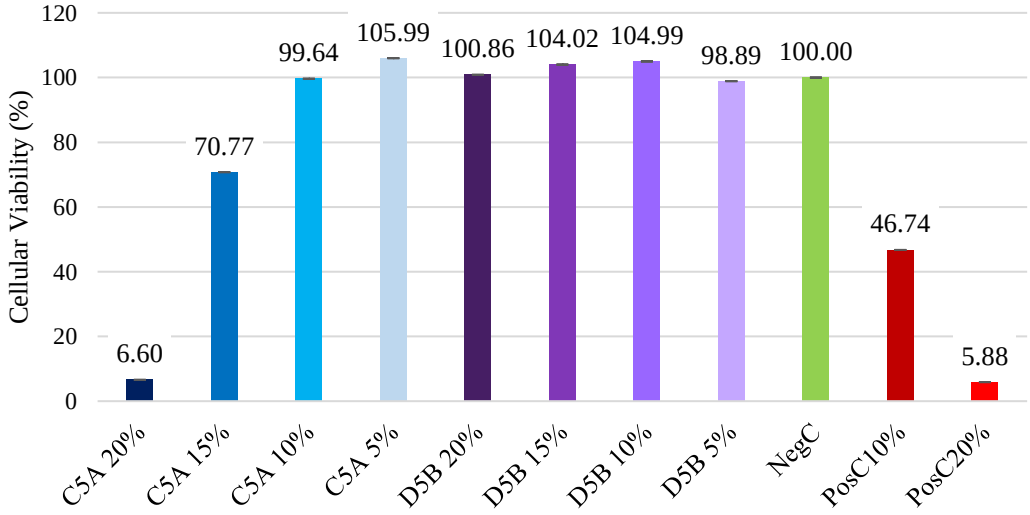

Figure 4.26 - Relative Cell Viability of Samples C5A and D5B

This time it was found that concentrations of 20 % were fatal for sample C while concentrations of 15 % were only slightly toxic, having gotten a much better result than in the first test. All concentrations of sample D were non-cytotoxic while for sample C only 10 % and 5 % were non-cytotoxic.

While the result of the first test would indicate the cell toxicity to be due to a common component, the second test shows the opposite. Assuming the first case was due to ethanol then it is possible that the second results could be due to the Sodium Alginate or $CaSO_4$ content of the C sample.

Lee & Mooney (2012, p. 3) state that "The immunogenic response at the injection or implantation sites might be attributed to impurities remaining in the alginate." It also states that "no significant inflammatory response was observed when gels formed from commercially available, highly purified alginate have been subcutaneously injected". According to Pithon et al., 2012 alginate can affect the ability of cells to multiply, being toxic enough to inhibit cell growth. It is also stated that repeated contacts with the material may result in a late toxic or allergic reaction. On the other hand, Calcium Sulphate has been used to repair bone defects due to its osteogenesis stimulating properties which indicate it has no adverse effect on cell growth [42].

The findings in the mentioned articles would suggest that, while there is a possibility that cytotoxicity was caused by Sodium Alginate, it is far more likely that it was caused by the absorption of ethanol during the sterilization phase and that the hydrogel with SA (protocol B) retained it for longer than the hydrogel with PVA (protocol D). If caused by SA, the obvious solution would be to use it in a smaller percentage since C samples showed no cytotoxicity at 10 % and 5 %. If, on the other hand, the cytotoxicity derives from the absorption of ethanol during sterilization, then a possible solution would be to increase the evaporation time.

5

5 Conclusions

This work had as an objective the development of a 3D printable polymeric material with shape memory properties. These objectives were only partially met since it was not possible to test the printed materials' shape memory properties. However, the materials were proved to be biocompatible, strong and flexible enough to be used in implants placed in a non-invasive way.

Several materials were used to try and develop a copolymer with the desired features. We started with the polymer PEGDA and used BAPO as the photoinitiator with either Sodium Alginate and $CaSO_4$ or PVA. Later BAPO was replaced with B2VT. Several photoinitiator concentrations were tested, as well as PVA concentrations.

Compression and tensile tests were done for the two main polymer mixtures studied – PEGDA/B2VT/SA/CaSO4 and PEGDA/B2VT/PVA. Tensile studies concluded that a higher percentage of PVA and B2VT influence the material, increasing the Young's Modulus.

Only the polymer mixture B material could be printed in an extrusion 3D printer. Unfortunately, it started to quickly break into pieces and dissolve when placed in water or simulated body fluid (SBF), meaning that it cannot be used on its own for implantable prostheses, requiring a hydrophobic coating. A PVA coating was suggested but requires more testing.

The introduction of SA in the PEGDA/B2VT base material and its extrusion printing caused the material to behave like a foam in the compression tests. The different laser powers used to reticulate this material did not produce significantly altered *E* values, although there seems to be a slight increase in samples reticulated at 941 mW

Cytotoxicity testing revealed some cell toxicity at higher concentrations of the B type material. While there is a possibility that cytotoxicity was caused by Sodium Alginate, it is far more likely that it was caused by the absorption of ethanol during the sterilization phase and

that the hydrogel with SA (polymer mixture B) retained it for longer than the hydrogel with PVA (polymer mixture D).

As always in scientific investigation, a lot more could be done in terms of testing new materials or component percentages. The most important thing would be to guarantee that the polymer mixture B material stopped dissolving in water. Since the thermal properties of the materials were not tested, this would also be necessary. Another interesting area to develop is the 3D printing of PVA hydrogels since this was not possible.

Bibliography

[1] Chia H N and Wu B M 2015 Recent advances in 3D printing of biomaterials *J. Biol. Eng.* **9**

[2] Webb E M, Elicker B M and Webb W R 2000 Using CT to Diagnose Nonneoplastic Tracheal Abnormalities *Am. J. Roentgenol.* **174** 1315–21

[3] Grillo H C 2002 Tracheal Replacement: A Critical Review Requirements for Replacement *Ann Thorac Surg* **73** 1995–2004

[4] Neville W E 1982 Reconstruction of the trachea and stem bronchi with Neville prosthesis. *Int. Surg.* **67** 229–34

[5] Neville W E, Bolanowski P J and Soltanzadeh H 1976 Prosthetic reconstruction of the trachea and carina. *J. Thorac. Cardiovasc. Surg.* **72** 525–38

[6] Minamoto H, Terra R M and Cardoso P F G 2011 Estenoses benignas da via aérea: tratamento endoscópico Benign airway stenosis: endoscopic treatment *Pulmão RJ* **20** 48–53

[7] Sugarbaker D J 2018 Técnicas diagnósticas e terapêuticas invasivas na doença pulmonar – Raphael Bueno David J Sugarbak

[8] Chang J W, Park S A, Park J-K, Choi J W, Kim Y-S, Shin Y S and Kim C-H 2014 Tissue-Engineered Tracheal Reconstruction Using Three-Dimensionally Printed Artificial Tracheal Graft: Preliminary Report *Artif. Organs* **38** E95–105

[9] Fanous N, Husain S A, Ruzmetov M, Rodefeld M D, Turrentine M W and Brown J W 2010 Anterior pericardial tracheoplasty for long-segment tracheal stenosis: Long-term outcomes *J. Thorac. Cardiovasc. Surg.* **139** 18–25

[10] Wurtz A, Porte H, Conti M, Dusson C, Desbordes J, Copin M-C and Marquette C-H 2010 Surgical technique and results of tracheal and carinal replacement with aortic allografts for salivary gland–type carcinoma *J. Thorac. Cardiovasc. Surg.* **140** 387–393.e2

[11] Wurtz A, Hysi I, Kipnis E, Zawadzki C, Hubert T, Jashari R, Copin M-C and Jude B 2013 Tracheal reconstruction with a composite graft: fascial flap-wrapped allogenic aorta with external cartilage-ring support *Interact. Cardiovasc. Thorac. Surg.* **16** 37–43

[12] Toomes H, Mickisch G and Vogt-Moykopf I 1985 Experiences with prosthetic reconstruction of the trachea and bifurcation. *Thorax* **40** 32–7

[13] Virk J S, Zhang H, Nouraei R, Sandhu G and Prosthetic S G 2017 Prosthetic reconstruction of the trachea: A historical perspective *World J Clin Cases* **5**

[14] Bao M, Lou X, Zhou Q, Dong W, Yuan H and Zhang Y 2014 Electrospun biomimetic fibrous scaffold from shape memory polymer of PDLLA- co -TMC for bone tissue engineering *ACS Appl. Mater. Interfaces* **6** 2611–21

[15] El Feninat F, Laroche G, Fiset M and Mantovani D 2002 Shape memory materials for biomedical applications *Adv. Eng. Mater.* **4** 91–104

[16] Sun J and Tan H 2013 Alginate-based biomaterials for regenerative medicine applications *Materials (Basel).* **6** 1285–309

[17] Lee K Y and Mooney D J 2012 Alginate: Properties and biomedical applications *Prog. Polym. Sci.*

[18] Dargaville B L, Vaquette C, Peng H, Rasoul F, Chau Y Q, Cooper-White J J, Campbell J H and Whittaker A K 2011 Cross-linked poly (trimethylene carbonate-co-L-lactide) as a biodegradable, elastomeric scaffold for vascular engineering applications *Biomacromolecules* **12** 3856–69

[19] Li G, Zhang H, Fortin D, Xia H and Zhao Y 2015 Poly(vinyl alcohol)-Poly(ethylene glycol) Double-Network Hydrogel: A General Approach to Shape Memory and Self-Healing Functionalities *Langmuir* **31** 11709–16

[20] Hoffman A S 2012 Hydrogels for biomedical applications ☆ *Adv. Drug Deliv. Rev.* **64** 18–23

[21] Xuzhen Q, Qianqian H, Guanghui G and Shuang G 2015 Characterization of UV-curable Poly(ethylene glycol) Diacrylate Based Hydrogels *Chem. Res. Chin. Univ* **31** 1046–50

[22] Yang L Q, He B, Meng S, Zhang J Z, Li M, Guo J, Guan Y M, Li J X and Gu Z W 2013 Biodegradable cross-linked poly(trimethylene carbonate) networks for implant applications: Synthesis and properties *Polym. (United Kingdom)* **54** 2668–75

[23] Ifkovits J L and Burdick J A 2007 Review: Photopolymerizable and Degradable Biomaterials for Tissue Engineering Applications *Tissue Eng.* **13** 2369–85

[24] Nemir S, Hayenga H N and West J L 2010 PEGDA hydrogels with patterned elasticity: Novel tools for the study of cell response to substrate rigidity *Biotechnol. Bioeng.*

[25] Nguyen A K, Gittard S D, Koroleva A, Schlie S, Gaidukeviciute A, Chichkov B N and Narayan R J 2013 Two-photon polymerization of polyethylene glycol diacrylate scaffolds with riboflavin and triethanolamine used as a water-soluble photoinitiator. *Regen. Med.* **8** 725–38

[26] Chris Chiu C Liquid bis-acylphosphine oxide (BAPO) photoinitiators

[27] Tack P, Victor J, Gemmel P and Annemans L 2016 3D-printing techniques in a medical setting: a systematic literature review *Biomed. Eng. Online* **15**

[28] Hiller A, Borchers K, Tovar G E M and Southan A 2017 Impact of intermediate UV curing and yield stress of 3D printed poly(ethylene glycol) diacrylate hydrogels on interlayer connectivity and maximum build height *Addit. Manuf.* **18** 136–44

[29] Hong S, Sycks D, Chan H F ai, Lin S, Lopez G P, Guilak F, Leong K W and Zhao X 2015 3D Printing: 3D Printing of Highly Stretchable and Tough Hydrogels into Complex, Cellularized Structures *Adv. Mater.*

[30] Hockaday L A, Kang K H, Colangelo N W, Cheung P Y C, Duan B, Malone E, Wu J, Girardi L N, Bonassar L J, Lipson H, Chu C C and Butcher J T 2012 Rapid 3D printing of anatomically accurate and mechanically heterogeneous aortic valve hydrogel scaffolds *IOP Publ. BIOFABRICATION Biofabrication* **4** 35005–12

[31] Markstedt K, Mantas A, Tournier I, Martínez Ávila H, Hägg D and Gatenholm P 2015 3D

Bioprinting Human Chondrocytes with Nanocellulose–Alginate Bioink for Cartilage Tissue Engineering Applications *Biomacromolecules* **16** 1489–96

[32] Hoch E, Tovar G E M and Borchers K 2014 Bioprinting of artificial blood vessels: current approaches towards a demanding goal *Eur. J. Cardio-Thoracic Surg.* **46** 767–78

[33] Fedorovich N E, Swennen I, Girones J, Moroni L, van Blitterswijk C A, Schacht E, Alblas J and Dhert W J A 2009 Evaluation of Photocrosslinked Lutrol Hydrogel for Tissue Printing Applications *Biomacromolecules* **10** 1689–96

[34] Verterra R 2018 Stress-Strain Diagram | Strength of Materials Review *MATHalino.com - Pinoy Math Community*

[35] Ashby M . 2006 The properties of foams and lattices *Philos. Trans. R. Soc. A Math. Phys. Eng. Sci.* **364** 15–30

[36] Simon Z 2015 Quasistatic Material Testing - AAC *AAc - Aerosp. Adv. Compos.*

[37] Li H, Chang J, Qin Y, Wu Y, Yuan M and Zhang Y 2014 Poly(lactide-co-trimethylene carbonate) and polylactide/polytrimethylene carbonate blown films *Int. J. Mol. Sci.*

[38] Ma Z, Wu Y, Wang J and Liu C 2017 In vitro and in vivo degradation behavior of poly(trimethylene carbonate-co-d,l-lactic acid) copolymer. *Regen. Biomater.* **4** 207–13

[39] Mondal D, Mollick M M R, Bhowmick B, Maity D, Bain M K, Rana D, Mukhopadhyay A, Dana K and Chattopadhyay D 2013 Effect of poly(vinyl pyrrolidone) on the morphology and physical properties of poly(vinyl alcohol)/sodium montmorillonite nanocomposite films *Prog. Nat. Sci. Mater. Int.* **23** 579–87

[40] Krimm S, Liang C Y and Sutherland G B B M 1956 Infrared spectra of high polymers. V. Polyvinyl alcohol *J. Polym. Sci.* **22** 227–47

[41] Pithon M M, Lacerda R, Santos D, Martins F O, Teresa M and Romanos V 2012 Cytotoxicity of alginate for orthodontic use *Dent. Press J Orthod. Dent. Press J. Orthod. Dent. Press J Orthod* **17211721** 1–5

[42] Beeson W H 1981 Plaster of Paris as an Alloplastic Implant in the Frontal Sinus *Arch. Otolaryngol.* **107** 664–9

Appendix

ANNEXE A

Mechanical tests performed:

As has been described in section 3.3.1, Young's Modulus is determined by the slope of the linear regression, in the elastic regime, and the Tensile Strength corresponds to the Maximum Stress that the material could withstand before breaking.

D3

The stress-strain curves of D3A membranes are represented in figure A.1 and the corresponding mechanical properties are represented in table A.1. In average, Young's Modulus for these membranes is of 2.43 (± 0.72) MPa and the Maximum Stress is of 0.62 (± 0.21) MPa.

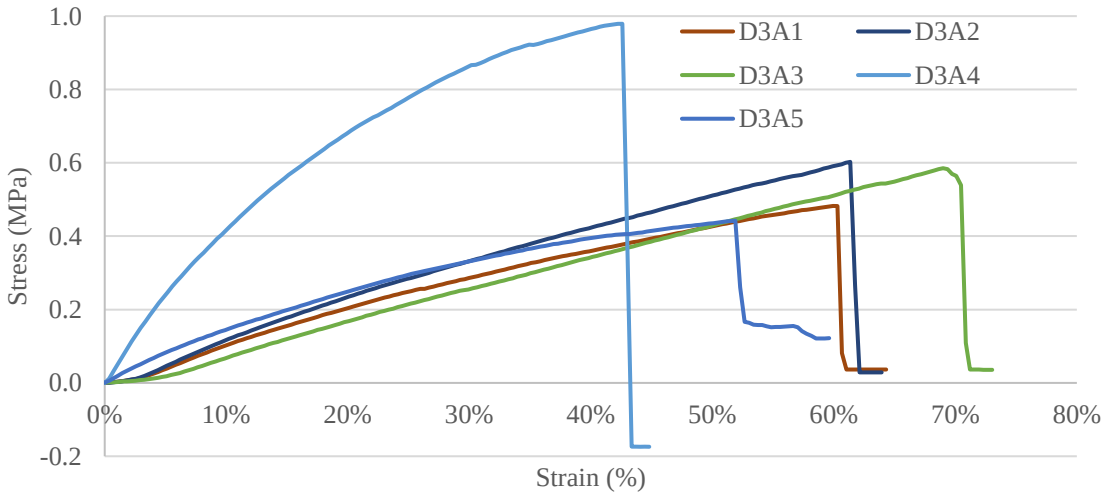

Figure A. 1 - D3A Stress-Strain Curves - Traction

Table A. 1 - Mechanical Properties of each D3A sample

Sample	Young's Modulus (MPa)	Max Stress (MPa)	Max Strain (%)	Max Force (kg)	Initial Distance (mm)
D3A1	1.85	0.48	60%	0.63	12.3
D3A2	2.67	0.60	61%	0.57	12.3
D3A3	2.84	0.59	69%	0.56	12.3
D3A4	3.27	0.98	43%	0.94	12.3
D3A5	1.54	0.44	52%	0.57	12.3
Average	2.43	0.62	57%	0.65	12.3
STD	0.72	0.21	9%	0.16	0

The stress-strain curves of D3B membranes are represented in figure A.2 and the corresponding mechanical properties are represented in table A.2. In average, Young's Modulus for these membranes is of 2.70 (± 0.51) MPa and the Maximum Stress is of 0.66 (± 0.18) MPa.

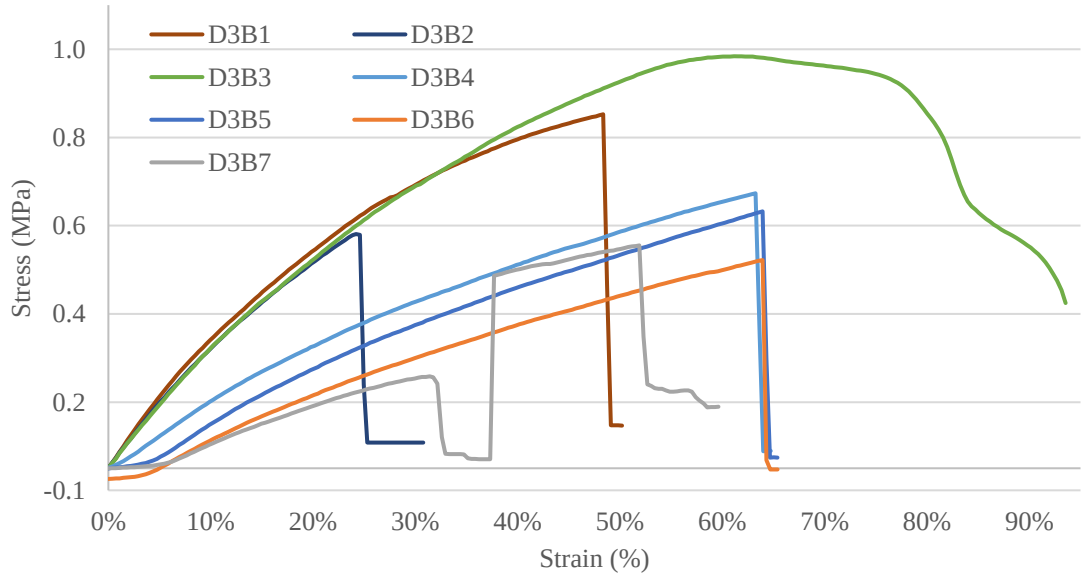

Figure 4. 2 - D3B Stress-Strain Curves - Traction

Table A. 2 - Mechanical Properties of each D3B sample

Sample	Young's Modulus (MPa)	Max Stress (MPa)	Max Strain (%)	Max Force (kg)	Initial Distance (mm)
D3B1	2.70	0.80	48%	0.84	12.3
D3B2	2.99	0.53	24%	0.52	12.3
D3B3	3.39	0.93	62%	0.93	12.3
D3B4	2.13	0.62	63%	0.59	12.3
D3B5	2.31	0.58	64%	0.59	12.3
D3B6	2.06	0.47	64%	0.56	12.3
D3B7	1.23	0.51	31%	0.57	12.3
Average	2.70	0.66	51%	0.67	12.3
STD	0.51	0.18	16%	0.17	0

The stress-strain curves of D3C membranes are represented in figure A.3 and the corresponding mechanical properties are represented in table A.3. In average, Young's Modulus for these membranes is of 1.41 (± 0.89) MPa and the Maximum Stress is of 0.44 (± 0.31) MPa.

D3C2 was from a different batch than the other D3C samples.

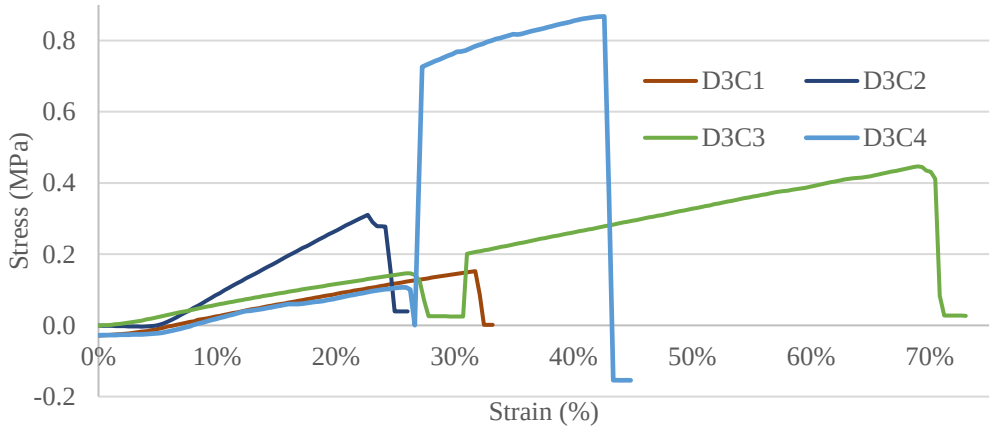

Figure A. 3 - D3C Stress-Strain Curves - Traction

Table A. 3 - Mechanical Properties of each D3C sample

Sample	Young's Modulus (MPa)	Max Stress (MPa)	Max Strain (%)	Max Force (kg)	Initial Distance (mm)
D3C1	1.02	0.15	32%	0.16	12.3
D3C2	2.74	0.31	23%	0.26	12.3
D3C3	0.89	0.45	26%	0.56	12.3
D3C4	0.99	0.87	26%	0.94	12.3
Average	1.41	0.44	27%	0.48	12.3
STD	0.89	0.31	3%	0.35	0

The stress-strain curves of D3Ct membranes are represented in figure A.4 and the corresponding mechanical properties are represented in table A.4. In average, Young's Modulus for these membranes is of 2.40 (± 0.25) MPa and the Maximum Stress is of 0.61 (± 0.44) MPa.

t: Tensile tests were performed a week after the films were reticulated which lead to t samples being smaller in size compared to other samples, probably due to water loss.

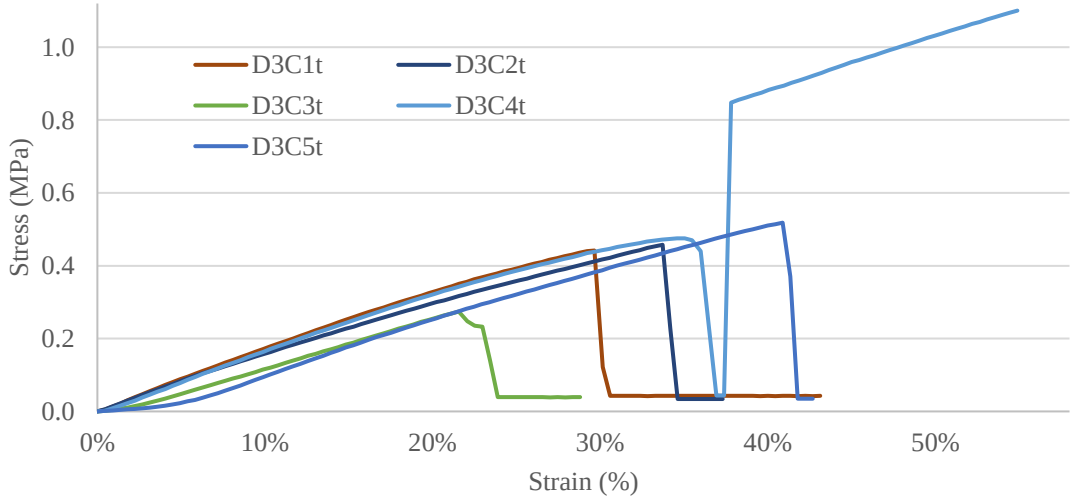

Figure A. 4 - D3Ct Stress-Strain Curves - Traction

Table A. 4 - Mechanical Properties of each D3Ct sample

Sample	Young's Modulus (MPa)	Max Stress (MPa)	Max Strain (%)	Max Force (kg)	Initial Distance (mm)
D3C1t	2.37	0.44	30%	0.25	10
D3C2t	2.35	0.46	34%	0.30	10
D3C3t	2.17	0.27	22%	0.16	10
D3C4t	2.30	1.38	35%	0.59	10
D3C5t	2.82	0.52	41%	0.32	10
Average	2.40	0.61	32%	0.32	10
STD	0.25	0.44	6%	0.16	0

The average mechanical properties of D3 samples are represented in table A.5. We can see a stable Young's Modulus and Maximum Stress with 3 mL of B2VT, despite the decrease in overall PVA percentage (A = 25 %; B = 15 %; C = 5 %). There is an accentuated decrease in Maximum Strain. Smaller samples (t) seem to give higher results in all properties except Maximum Force (kg) than longer samples made in the same conditions.

Table A. 5 - Average Mechanical Properties of D3 samples

Sample	Young's Modulus (MPascal)	Max Stress (MPascal)	Max Strain (%)	Max Force (kg)	Initial Distance (mm)
D3A	2.43	0.62	57%	0.65	12.3
D3B	2.70	0.66	51%	0.67	12.3
D3C	1.41	0.44	27%	0.48	12.3
D3Ct	2.40	0.61	32%	0.32	10

D4

The stress-strain curves of D4A membranes are represented in figure A.5 and the corresponding mechanical properties are represented in table A.6. In average, Young's Modulus for these membranes is of 2.32 (± 0.55) MPa and the Maximum Stress is of 0.49 (± 0.16) MPa.

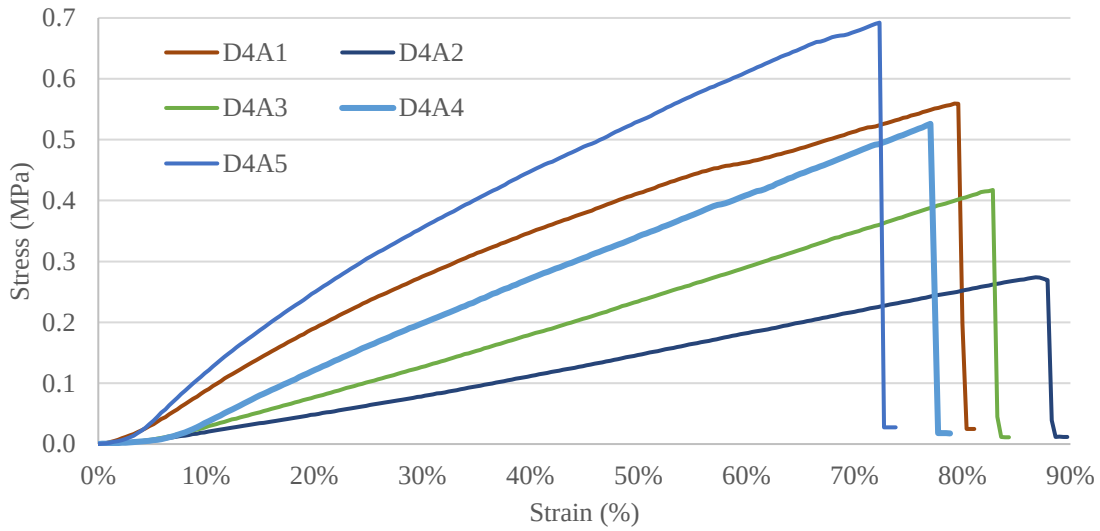

Figure 4. 5 - D4A Stress-Strain Curves - Traction

Table A. 6 - Mechanical Properties of each D4A sample

Sample	Young's Modulus (MPa)	Max Stress (MPa)	Max Strain (%)	Max Force (kg)	Initial Distance (mm)
D4A1	2.36	0.56	79%	0.61	12.3
D4A2	1.48	0.27	87%	0.33	12.3
D4A3	2.18	0.42	83%	0.44	12.3
D4A4	2.66	0.53	77%	0.36	12.3
D4A5	2.90	0.69	72%	0.60	12.3
Average	2.32	0.49	80%	0.47	12.3
STD	0.55	0.16	5%	0.13	0

The stress-strain curves of D4B membranes are represented in figure A.6 and the corresponding mechanical properties are represented in table A.7. In average, Young's Modulus for these membranes is of 2.94 (± 0.67) MPa and the Maximum Stress is of 0.71 (± 0.25) MPa.

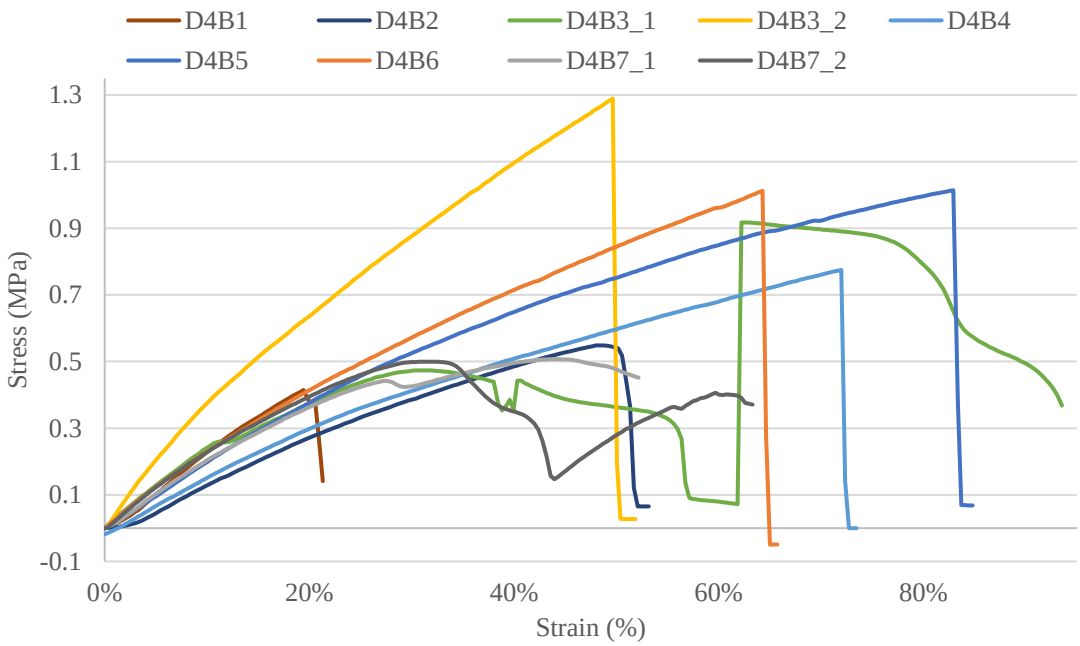

Figure A. 6 - D4B Stress-Strain Curves - Traction

Table A. 7 - Mechanical Properties of each D4B sample

Sample	Young's Modulus (MPa)	Max Stress (MPa)	Max Strain (%)	Max Force (kg)	Initial Distance (mm)
D4B1	2.92	0.41	19%	0.39	12.3
D4B2	2.43	0.55	48%	0.82	12.3
D4B3_1	2.38	0.92	31%	0.93	12.3
D4B3_2	5.63	1.29	50%	1.31	12.3
D4B4	3.10	0.77	72%	0.47	12.3
D4B5	3.65	1.01	83%	0.71	12.3
D4B6	4.16	1.01	64%	0.58	12.3
D4B7_1	2.39	0.51	44%	0.39	12.3
D4B7_2	2.48	0.50	31%	0.39	12.3
Average	3.35	0.85	49%	0.75	12.3
STD	1.21	0.30	21%	0.31	0
Average*	2.94	0.71	49%	0.59	12.3
STD*	0.67	0.25	22%	0.21	0

The stress-strain curves of D4C membranes are represented in figure A.7 and the corresponding mechanical properties are represented in table A.8. In average, Young's Modulus for these membranes is of 1.43 (± 0.23) MPa and the Maximum Stress is of 0.28 (± 0.15) MPa.

Samples D4C4, D4C5, and D4C6 were made at a different time than other D4C samples.

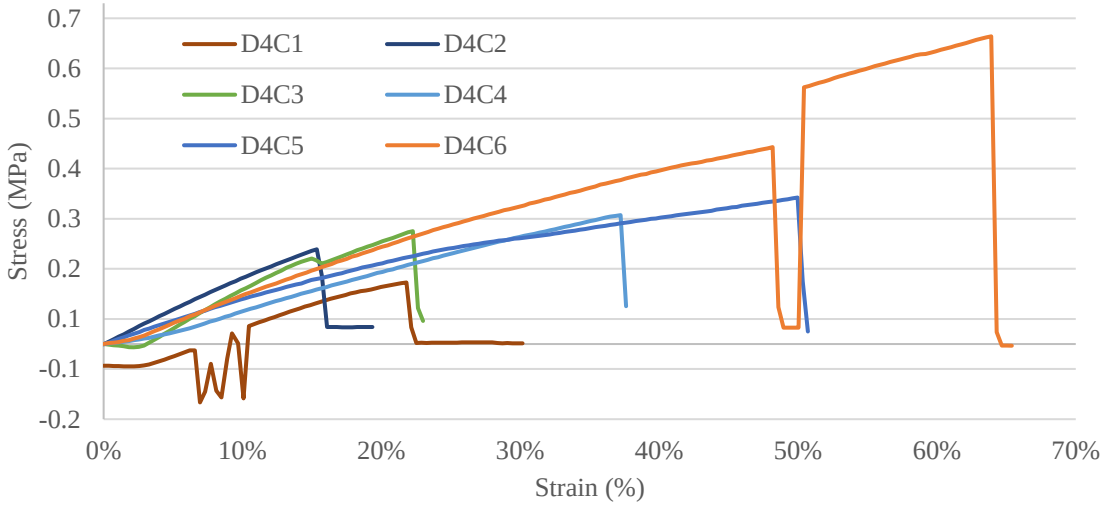

Figure A. 7 - D4C Stress-Strain Curves - Traction

Table A. 8 - Mechanical Properties of each D4C sample

Sample	Young's Modulus (MPa)	Max Stress (MPa)	Max Strain (%)	Max Force (kg)	Initial Distance (mm)
D4C1	1.14	0.12	22%	0.15	12.3
D4C2	1.55	0.19	15%	0.16	12.3
D4C3	1.65	0.23	22%	0.20	12.3
D4C4	1.36	0.26	37%	0.28	12.3
D4C5	1.17	0.29	50%	0.31	12.3
D4C6	1.72	0.61	48%	0.56	12.3
Average	1.43	0.28	32%	0.28	12.3
STD	0.23	0.17	13%	0.15	0

The stress-strain curves of D4Ct membranes are represented in figure A.8 and the corresponding mechanical properties are represented in table A.9. In average, Young's Modulus for these membranes is of 3.09 (± 0.52) MPa and the Maximum Stress is of 0.64 (± 0.18) MPa.

t: Tensile tests were performed a week after the films were reticulated which lead to t samples being smaller in size compared to other samples. probably due to water loss.

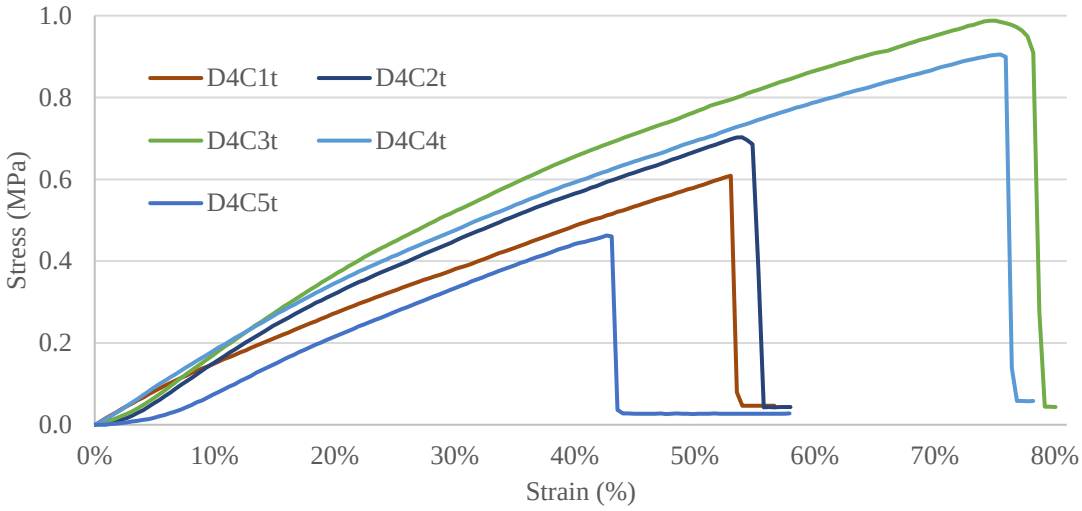

Figure A. 8 - D4Ct Stress-Strain Curves - Traction

Table 4. 9 - Mechanical Properties of each D4Ct sample

Sample	Young's Modulus (MPa)	Max Stress (MPa)	Max Strain (%)	Max Force (kg)	Initial Distance (mm)
D4C1t	2.78	0.61	53%	0.36	10
D4C2t	2.98	0.70	54%	0.44	10
D4C3t	3.71	0.50	75%	0.59	10
D4C4t	3.51	0.91	75%	0.45	10
D4C5t	2.46	0.46	43%	0.24	10
Average	3.09	0.64	60%	0.42	10
STD	0.52	0.18	13%	0.13	0

The average mechanical properties of D4 samples are represented in table A.10. We can see a slightly increasing Young's Modulus and Maximum Stress with 4 mL of B2VT, despite the decrease in overall PVA percentage (A = 25 %; B = 15 %; C = 5 %). There is an accentuated decrease in Maximum Strain if considering samples C4C. Smaller samples (t) seem to give significantly higher results in all properties than longer samples made under the same conditions.

Table A. 10 - Average Mechanical Properties of D4 samples

Sample	Young's Modulus (MPa)	Max Stress (MPa)	Max Strain (%)	Max Force (kg)	Initial Distance (mm)
D4A	2.32	0.49	80%	0.47	12.3
D4B	2.94	0.71	49%	0.59	12.3
D4C	1.43	0.28	32%	0.28	12.3
D4Ct	3.09	0.64	60%	0.42	10

D5

The stress-strain curves of D5A membranes are represented in figure A.9 and the corresponding mechanical properties are represented in table A.11. In average, Young's Modulus for these membranes is of 4.55 (± 1.31) MPa and the Maximum Stress is of 1.13 (± 0.37) MPa.

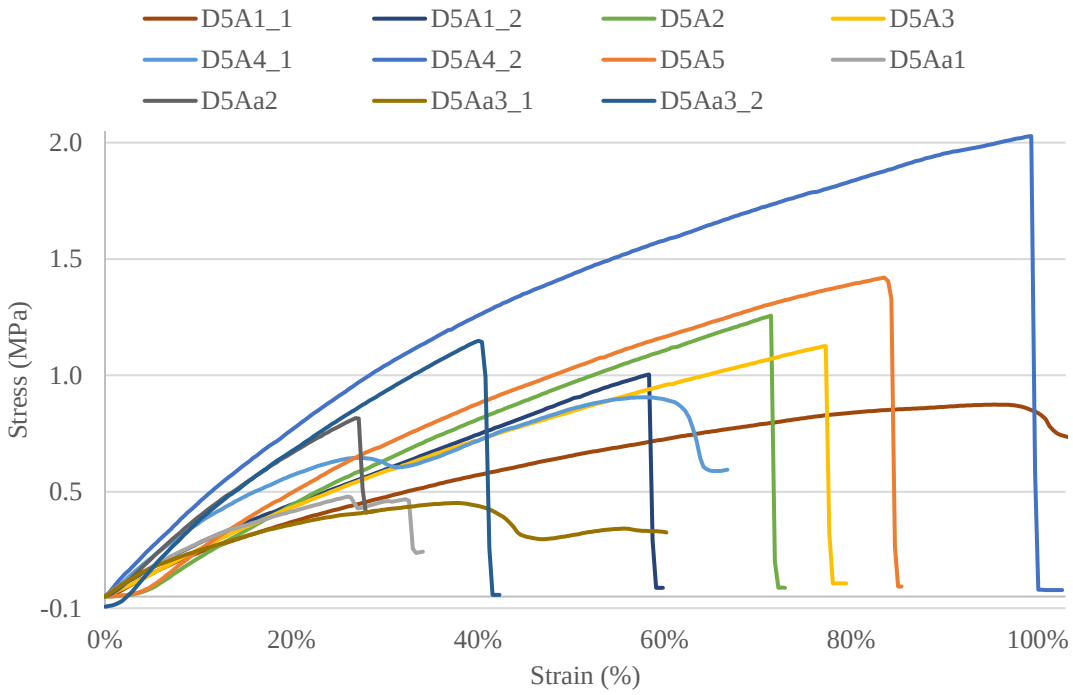

Figure A. 9 - D5A Stress-Strain Curves - Traction

Table A. 11 - Mechanical Properties of each D5A sample

Sample	Young's Modulus (MPa)	Max Stress (MPa)	Max Strain (%)	Max Force (kg)	Initial Distance (mm)
D5A1_1	2.69	0.82	95%	0.86	12.3
D5A1_2	4.40	0.95	58%	1.16	12.3
D5A2	5.06	1.21	71%	1.16	12.3
D5A3	4.24	1.08	77%	1.25	12.3
D5A4_1	2.88	0.86	58%	0.66	12.3
D5A4_2	6.97	1.98	99%	1.36	12.3
D5A5	5.30	1.37	83%	1.39	12.3
D5Aa1	2.07	0.43	26%	0.38	12.3
D5Aa2	4.21	0.77	27%	0.72	12.3
D5Aa3_1	1.38	0.40	37%	0.33	12.3
D5Aa3_2	5.23	1.10	40%	0.91	12.3
Average	4.20	1.05	61%	0.99	12.3
STD	1.51	0.44	25%	0.35	0
Average*	4.55	1.13	75%	1.05	12.3
STD*	1.31	0.37	14%	0.27	0

The stress-strain curves of D5B membranes are represented in figure A.10 and the corresponding mechanical properties are represented in table A.12. In average, Young's Modulus for these membranes is of 3.24 (± 0.89) MPa and the Maximum Stress is of 0.89 (± 0.19) MPa.

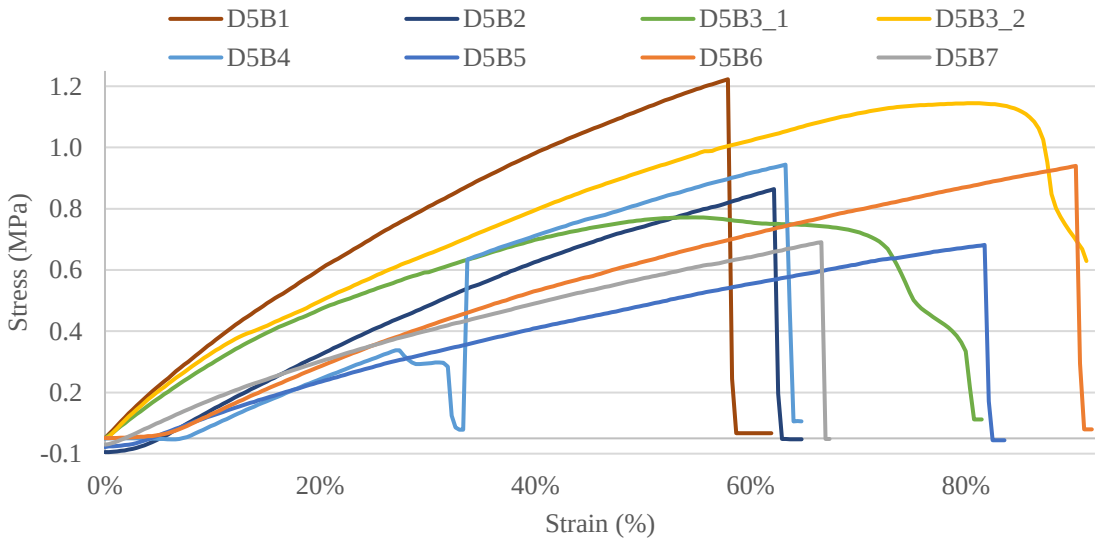

Figure A. 10 - D5B Stress-Strain Curves - Traction

Table A. 12 - Mechanical Properties of each D5B sample

Sample	Young's Modulus (MPa)	Max Stress (MPa)	Max Strain (%)	Max Force (kg)	Initial Distance (mm)
D5B1	4.53	1.17	58%	0.98	12.3
D5B2	3.45	0.81	62%	0.75	12.3
D5B3_1	2.60	0.72	55%	0.75	12.3
D5B3_2	3.94	1.09	81%	1.14	12.3
D5B4	2.24	0.89	27%	0.59	12.3
D5B5	2.67	0.63	82%	0.44	12.3
D5B6	3.54	0.89	90%	0.86	12.3
D5B7	2.56	0.64	67%	0.81	12.3
Average	3.24	0.89	65%	0.79	12.3
STD	0.89	0.19	16%	0.23	0

The stress-strain curves of D5C membranes are represented in figure A.11 and the corresponding mechanical properties are represented in table A.13. In average, Young's Modulus for these membranes is of 0.78 (± 0.04) MPa and the Maximum Stress is of 0.11 (± 0.04) MPa.

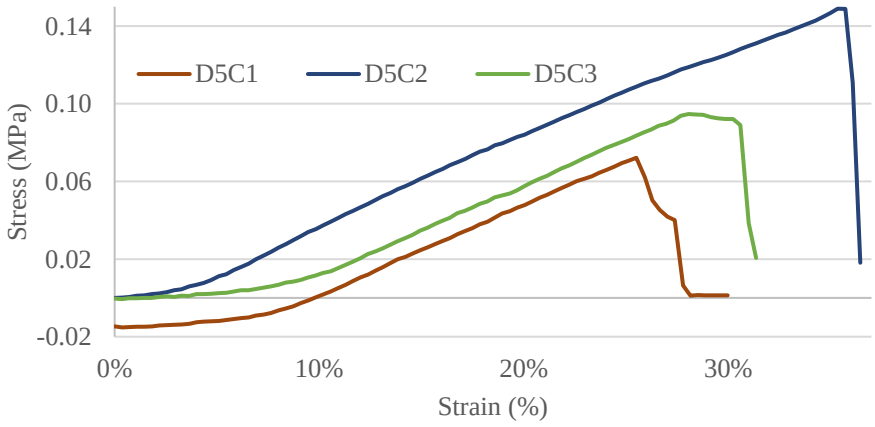

Figure A. 11 - D5C Stress-Strain Curves – Traction

Table A. 13 - Mechanical Properties of each D5C sample

Sample	Young's Modulus (MPa)	Max Stress (MPa)	Max Strain (%)	Max Force (kg)	Initial Distance (mm)
D5C1	0.74	0.07	26%	0.08	12.3
D5C2	0.81	0.15	35%	0.15	12.3
D5C3	0.80	0.09	28%	0.09	12.3
Average	0.78	0.11	30%	0.11	12.3
STD	0.04	0.04	4%	0.04	0

The stress-strain curves of D5Ct membranes are represented in figure 4.12 and the corresponding mechanical properties are represented in table 4.14. In average, Young's Modulus for these membranes is of 1.97 (± 0.41) MPa and the Maximum Stress is of 0.31 (± 0.07) MPa.

t: Tensile tests were performed a week after the films were reticulated which lead to t samples being smaller in size compared to other samples. probably due to water loss.

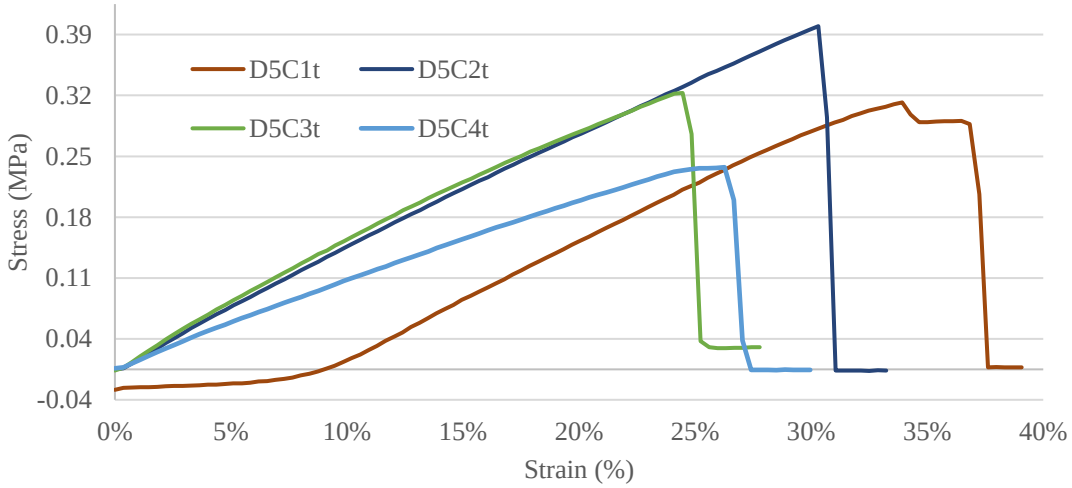

Figure A. 12 - D5Ct Stress-Strain Curves – Traction

Table A. 14 - Mechanical Properties of each D5Ct sample

Sample	Young's Modulus (MPa)	Max Stress (MPa)	Max Strain (%)	Max Force (kg)	Initial Distance (mm)
D5C1t	2.28	0.31	42%	0.19	10
D5C2t	2.29	0.39	37%	0.26	10
D5C3t	1.90	0.32	30%	0.22	10
D5C4t	1.43	0.23	32%	0.18	10
Average	1.97	0.31	35%	0.21	10
STD	0.41	0.07	5%	0.04	0

Annexe B

AC30

The stress-strain curves of AC30 membranes during perpendicular compression are represented in figure B.1 and the corresponding thicknesses (before and after compression and averages) are represented in figure B.2. The average thickness is 6.18 mm before and 6.65 mm after compression.

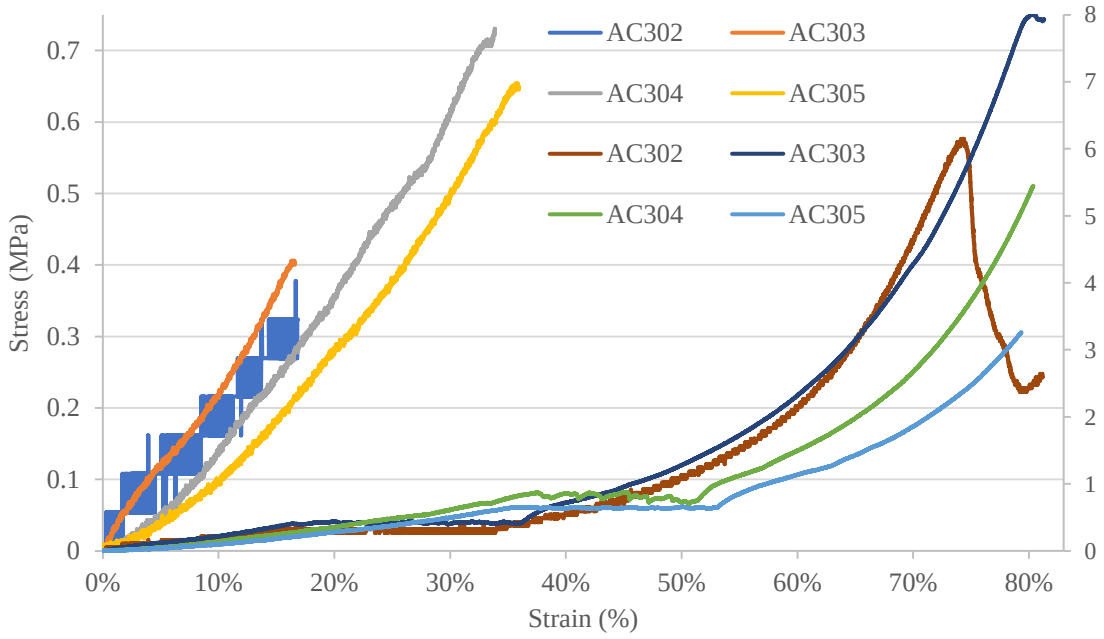

Figure B. 1 - Stress-Strain Curves for Perpendicular Compression Tests of Cubes Reticulated at 470 mW – first slope for each curve on the left axis and original curve for each sample on the right axis

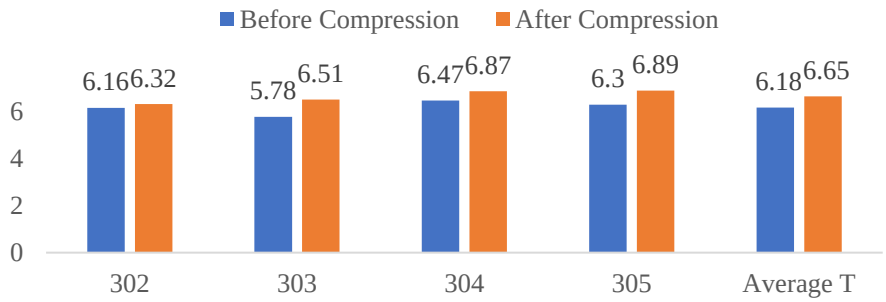

Figure B. 2 - Thickness Variation (mm) of each AC30 sample reticulated at 470 mW and their Average Thickness, before and after Perpendicular Compression

The stress-strain curves of AC30 membranes during parallel compression are represented in figure B.3 and the corresponding thicknesses (before and after compression and averages) are represented in figure B.4. The average thickness is 6.58 mm before and 6.46 mm after compression.

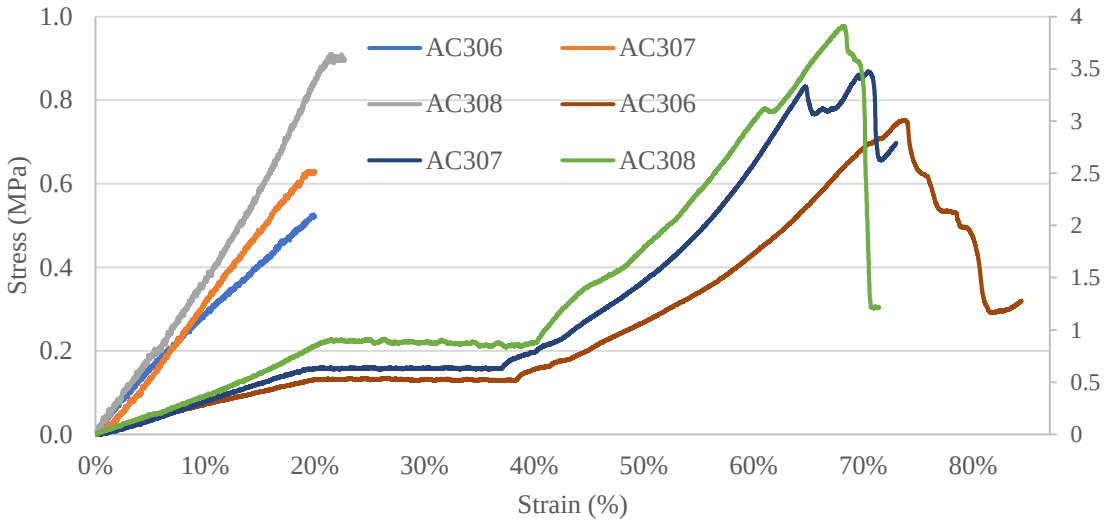

Figure B. 3 - Stress-Strain Curves for Parallel Compression Tests of Cubes Reticulated at 470 mW – first slope for each curve on the left axis and original curve for each sample on the right axis

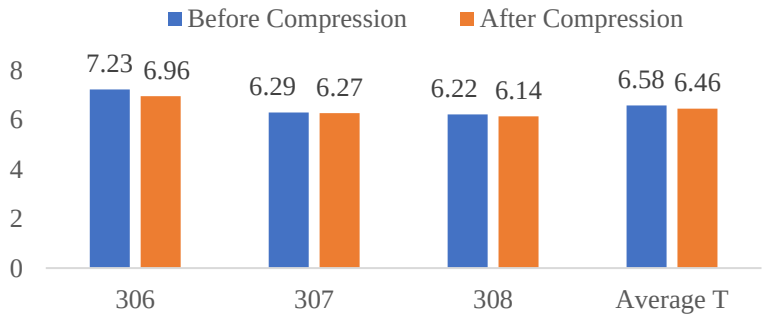

Figure B. 4 - Thickness Variation (mm) of each AC30 sample reticulated at 470 mW and their Average Thickness, before and after Parallel Compression

AC40

The stress-strain curves of AC40 membranes during perpendicular compression are represented in figure B.5 and the corresponding thicknesses (before and after compression and averages) are represented in figure B.6. The average thickness is 5.50 mm before and 5.34 mm after compression.

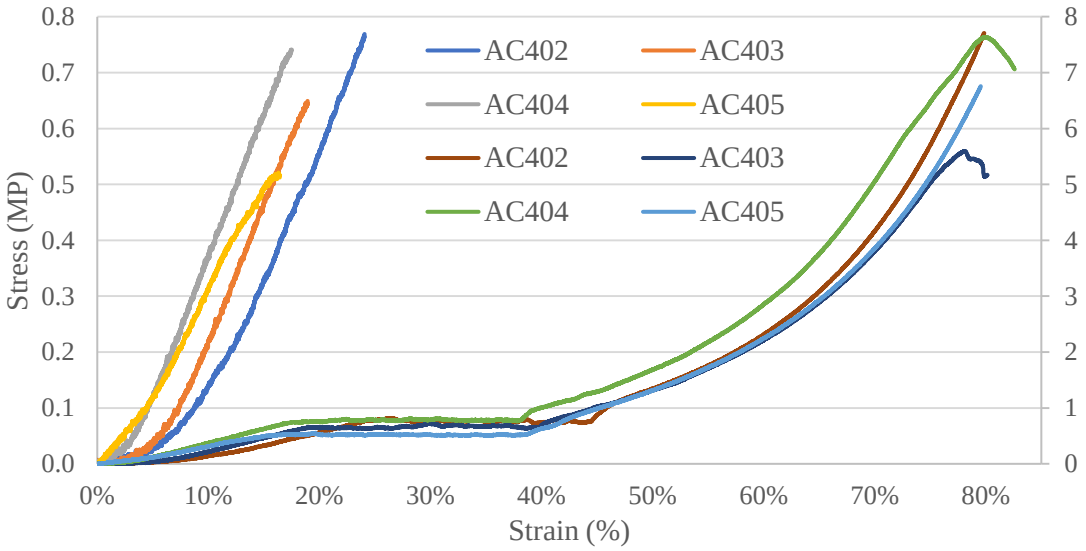

Figure B. 5 - Stress-Strain Curves for Perpendicular Compression Tests of Cubes Reticulated at 627 mW – first slope for each curve on the left axis and original curve for each sample on the right axis

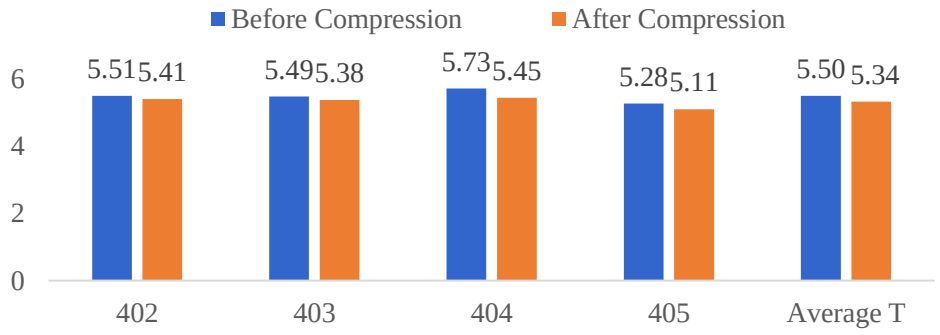

Figure B. 6 - Thickness Variation (mm) of each AC40 sample reticulated at 627 mW and their Average Thickness, before and after Perpendicular Compression

The stress-strain curves of AC40 membranes during parallel compression are represented in figure B.7 and the corresponding thicknesses (before and after compression and averages) are represented in figure B.8. The average thickness is 6.59 mm before and 6.35 mm after compression.

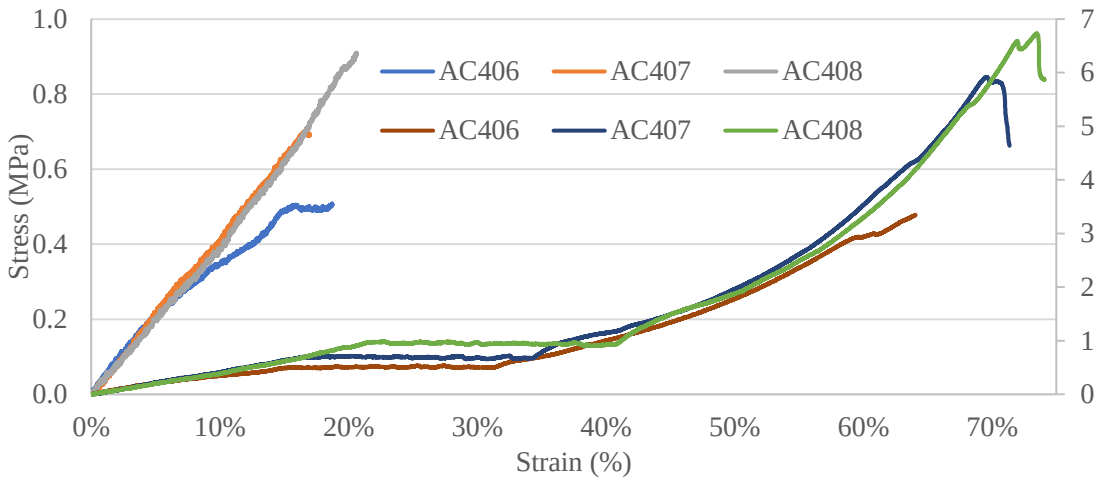

Figure B. 7 - Stress-Strain Curves for Parallel Compression Tests of Cubes Reticulated at 627 mW – first slope for each curve on the left axis and original curve for each sample on the right axis

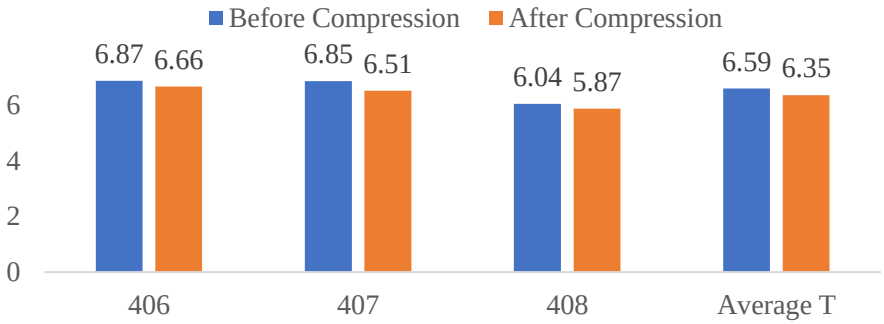

Figure B. 8 - Thickness Variation (mm) of each AC40 sample reticulated at 627 mW and their Average Thickness, before and after Parallel Compression

AC50

The stress-strain curves of AC50 membranes during perpendicular compression are represented in figure B.9 and the corresponding thicknesses (before and after compression and averages) are represented in figure B.10. The average thickness is 6.54 mm before and 5.37 mm after compression.

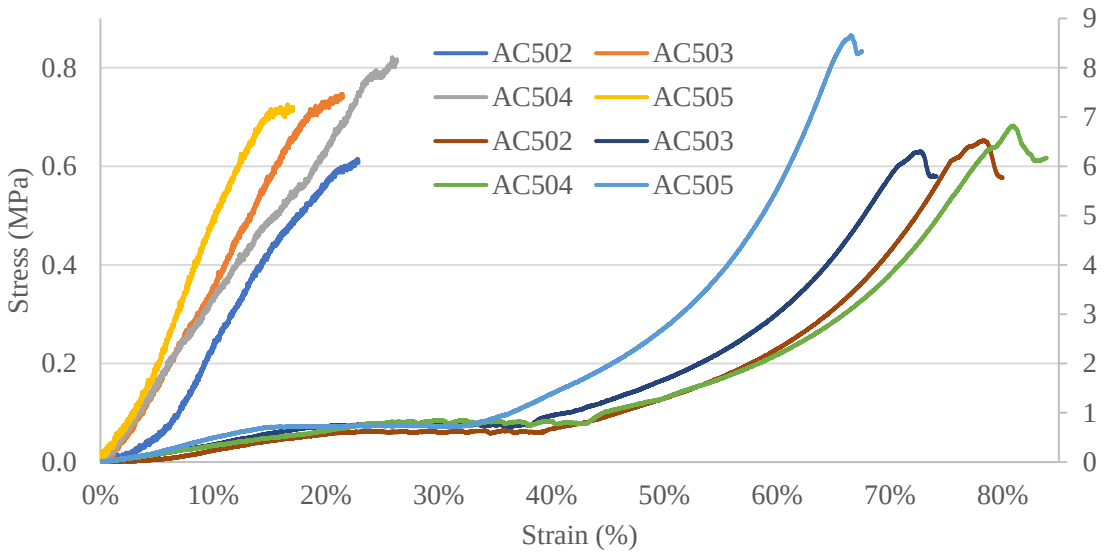

Figure B. 9 - Stress-Strain Curves for Perpendicular Compression Tests of Cubes Reticulated at 784 mW – first slope for each curve on the left axis and original curve for each sample on the right axis

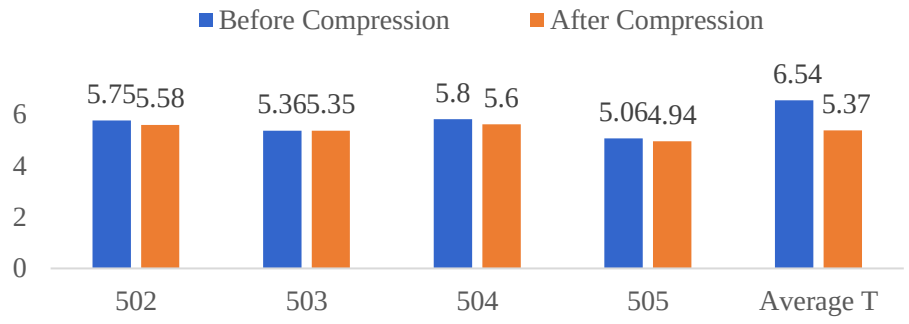

Figure B. 10 - Thickness Variation (mm) of each AC50 sample reticulated at 784 mW and their Average Thickness, before and after Perpendicular Compression

The stress-strain curves of AC50 membranes during parallel compression are represented in figure B.11 and the corresponding thicknesses (before and after compression and averages) are represented in figure B.12. The average thickness is 6.73 mm before and 6.85 mm after compression.

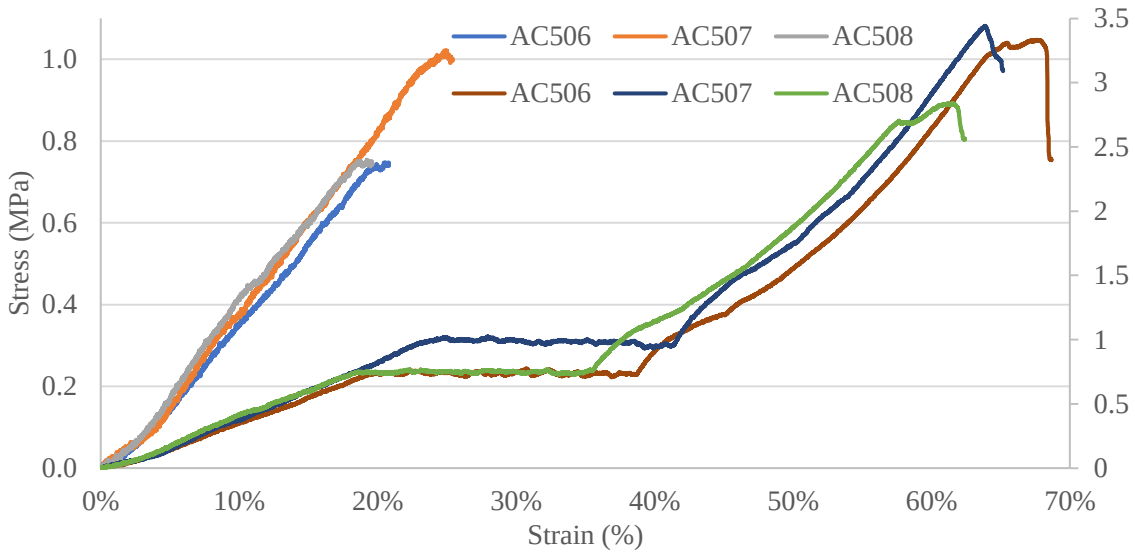

Figure B. 11 - Stress-Strain Curves for Parallel Compression Tests of Cubes Reticulated at 784 mW – first slope for each curve on the left axis and original curve for each sample on the right axis

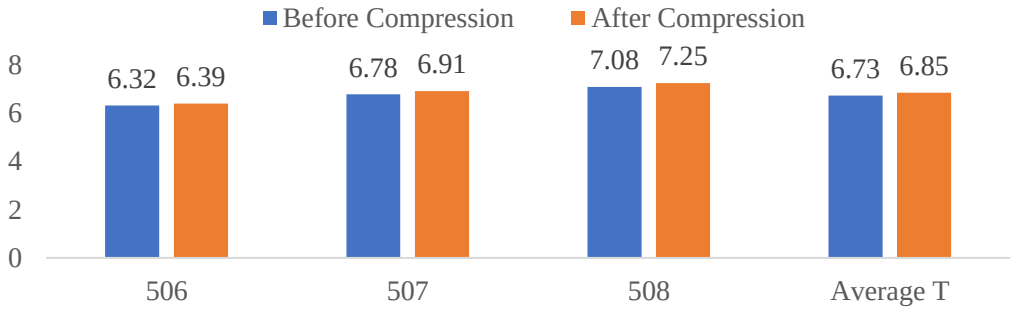

Figure B. 12 - Thickness Variation (mm) of each AC50 sample reticulated at 784 mW and their Average Thickness, before and after Parallel Compression

AC60

The stress-strain curves of AC60 membranes during perpendicular compression are represented in figure B.13 and the corresponding thicknesses (before and after compression and averages) are represented in figure B.14. The average thickness is 5.34 mm before and 5.22 mm after compression.

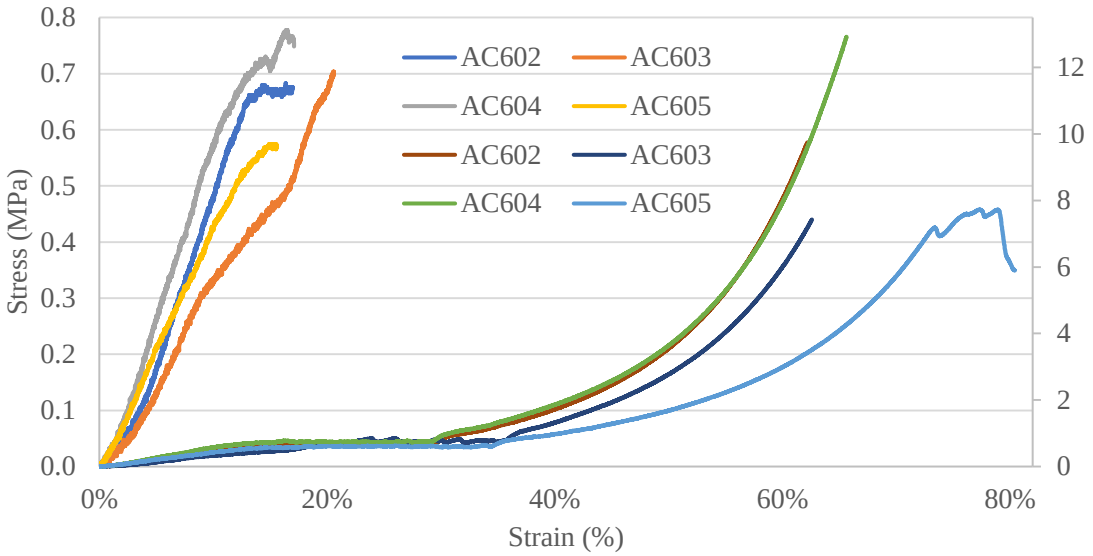

Figure B. 13 - Stress/ Strain Curves for Perpendicular Compression Tests of Cubes Reticulated at 941 mW – first slope for each curve on the left axis and original curve for each sample on the right axis

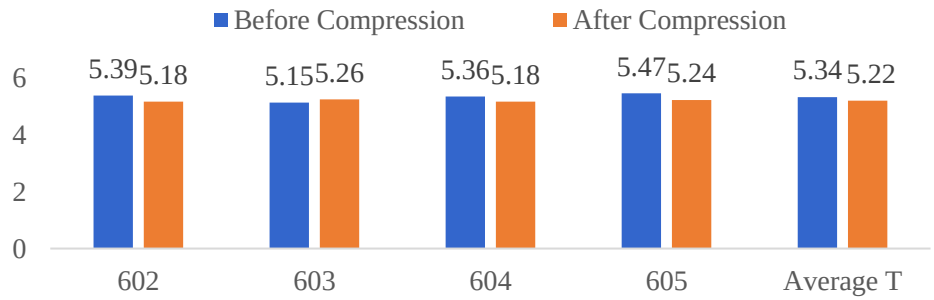

Figure B. 14 - Thickness Variation (mm) of each AC60 sample reticulated at 941 mW and their Average Thickness, before and after Perpendicular Compression

The stress-strain curves of AC60 membranes during parallel compression are represented in figure B.15 and the corresponding thicknesses (before and after compression and averages) are represented in figure B.16. The average thickness is 6.35 mm before and 6.19 mm after compression.

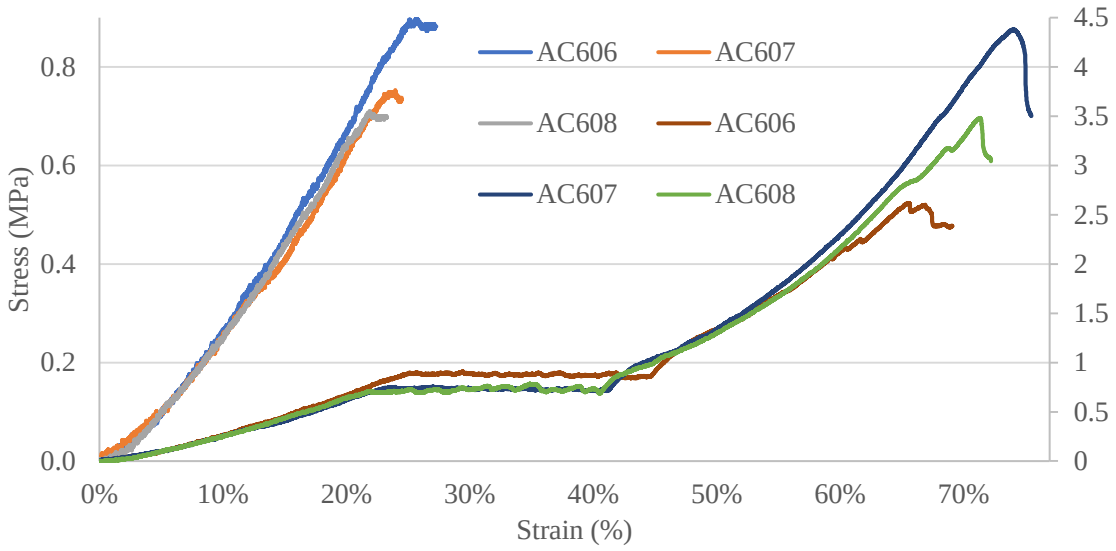

Figure B. 15 - Stress-Strain Curves for Parallel Compression Tests of Cubes Reticulated at 941 mW – first slope for each curve on the left axis and original curve for each sample on the right axis

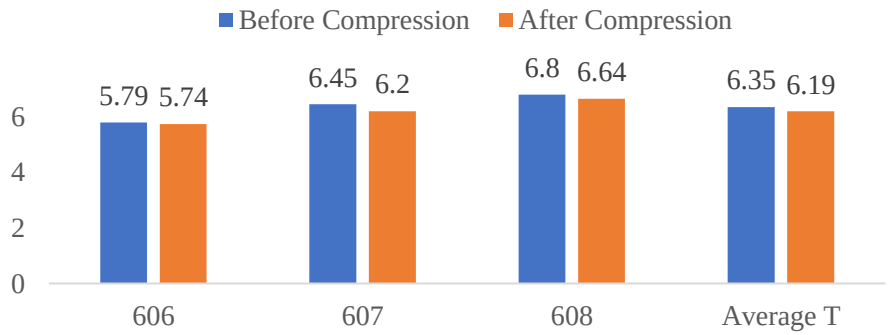

Figure B. 16 - Thickness Variation (mm) of each AC60 sample reticulated at 941 mW and their Average Thickness, before and after Parallel Compression

AC80

The stress-strain curves of AC80 membranes during perpendicular compression are represented in figure B.17 and the corresponding thicknesses (before and after compression and averages) are represented in figure B.18. The average thickness is 5.20 mm before and 5.09 mm after compression.

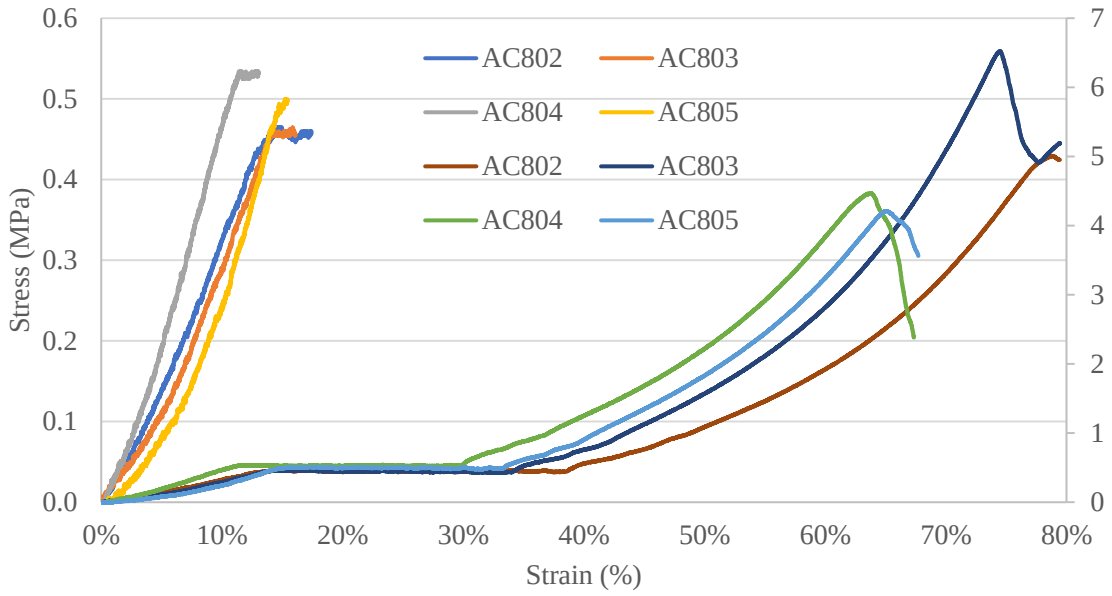

Figure B. 17 - Stress-Strain Curves for Perpendicular Compression Tests of Cubes Reticulated at 1255 mW – first slope for each curve on the left axis and original curve for each sample on the right axis

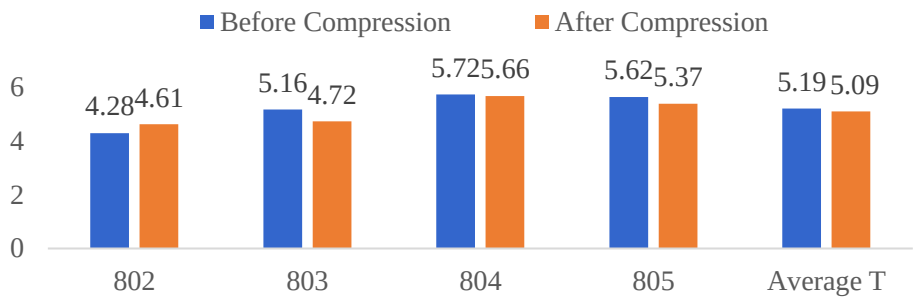

Figure B. 18 - Thickness Variation (mm) of each AC80 sample reticulated at 1255 mW and their Average Thickness, before and after Perpendicular Compression

The stress-strain curves of AC80 membranes during parallel compression are represented in figure B.19 and the corresponding thicknesses (before and after compression and averages) are represented in figure B.20. The average thickness is 6.64 mm before and 6.45 mm after compression.

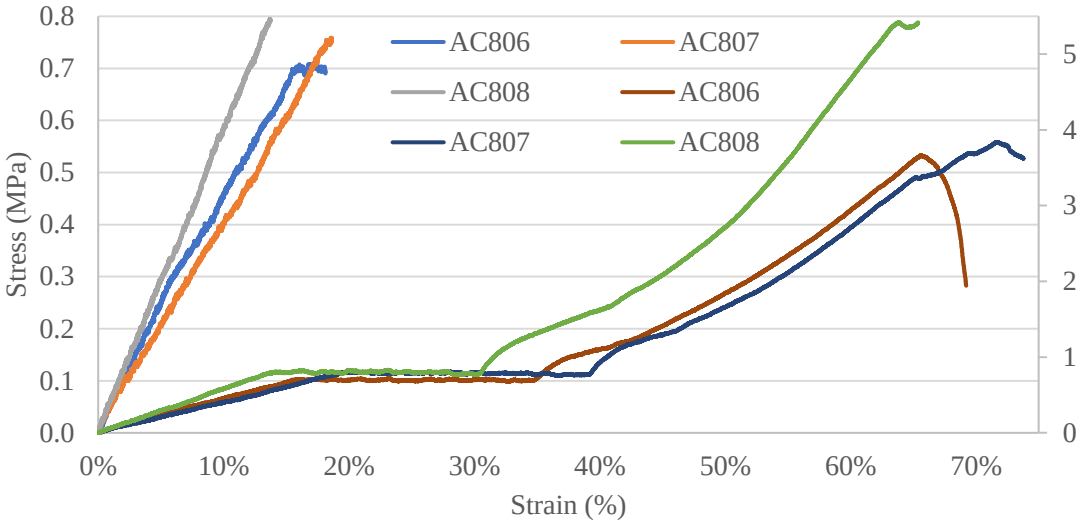

Figure B. 19 - Stress-Strain Curves for Parallel Compression Tests of Cubes Reticulated at 1255 mW – first slope for each curve on the left axis and original curve for each sample on the right axis

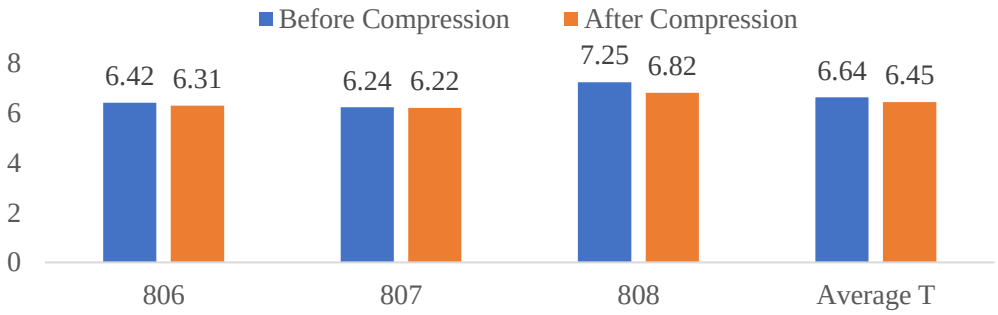

Figure B. 20 - Thickness Variation (mm) of each AC80 sample reticulated at 1255 mW and their Average Thickness, before and after Parallel Compression

AC100

The stress-strain curves of AC100 membranes during perpendicular compression are represented in figure B.21 and the corresponding thicknesses (before and after compression and averages) are represented in figure B.22. The average thickness is 4.83 mm before and 4.71 mm after compression.

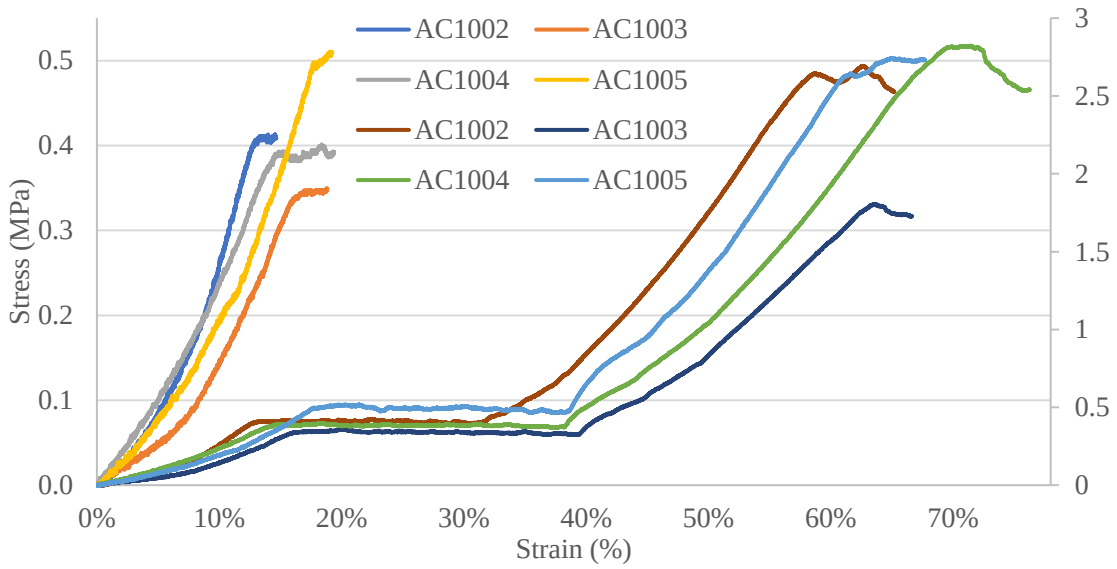

Figure B. 21 - Stress-Strain Curves for Perpendicular Compression Tests of Cubes Reticulated at 1569 mW – first slope for each curve on the left axis and original curve for each sample on the right axis

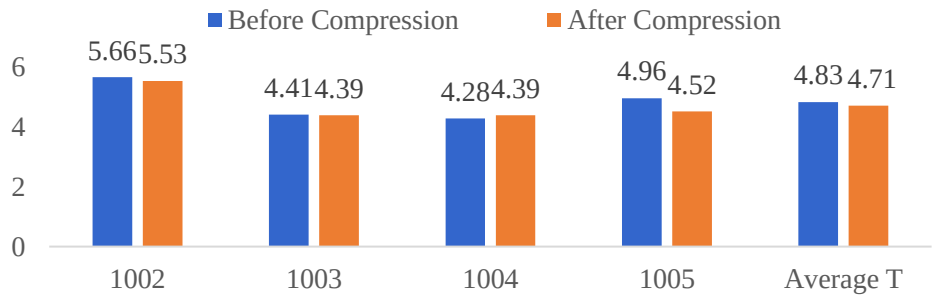

Figure B. 22 - Thickness Variation (mm) of each AC100 sample reticulated at 1569 mW and their Average Thickness, before and after Perpendicular Compression

The stress-strain curves of AC100 membranes during parallel compression are represented in figure B.23 and the corresponding thicknesses (before and after compression and averages) are represented in figure B.24. The average thickness is 7.31 mm before and 7.02 mm after compression.

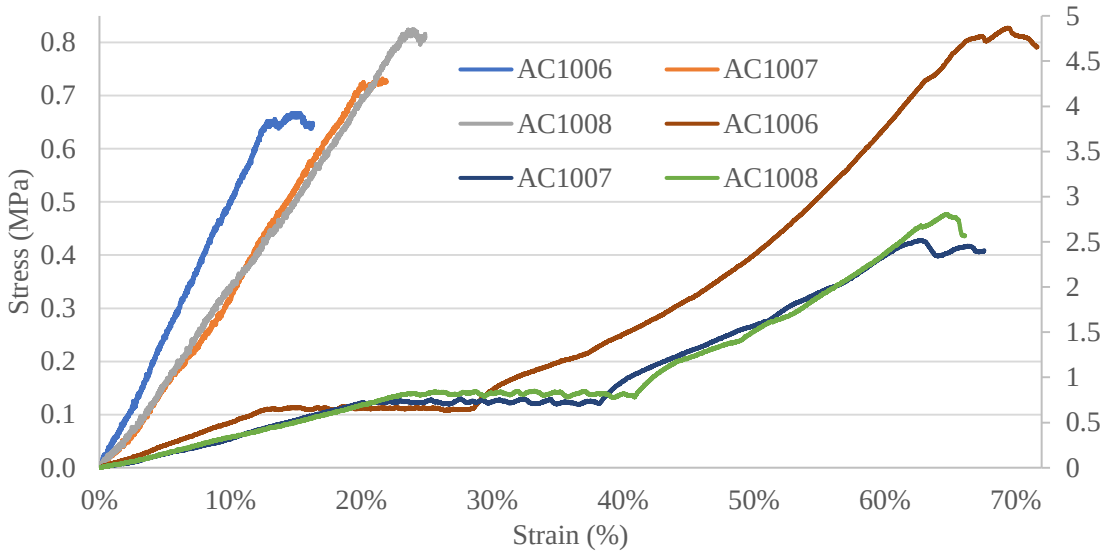

Figure B. 23 - Stress-Strain Curves for Parallel Compression Tests of Cubes Reticulated at 1569 mW – first slope for each curve on the left axis and original curve for each sample on the right axis

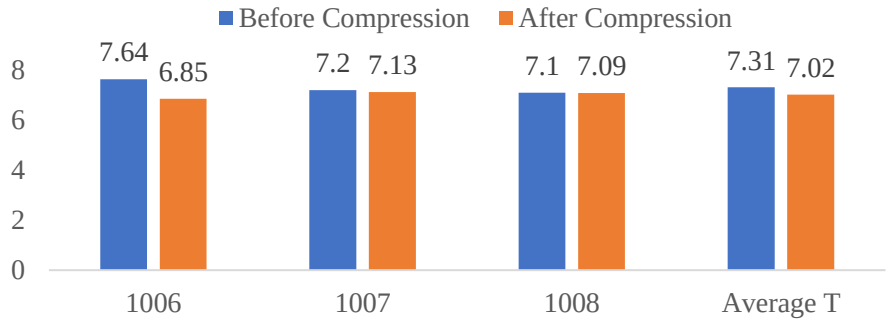

Figure B. 24 - Thickness Variation (mm) of each AC80 sample reticulated at 1255 mW and their Average Thickness, before and after Parallel Compression